Methods of diffusion MRI tractography for localization of the anterior optic pathway: A systematic review of validated methods

Alessandro Carrozzi [a,1], Laura Ludovica Gramegna [a,b,*,1], Giovanni Sighinolfi [a], Matteo Zoli [a,c], Diego Mazzatenta [a,c], Claudia Testa [d], Raffaele Lodi [a,e], Caterina Tonon [a,b], David Neil Manners [b,f]

[a] *Department of Biomedical and Neuromotor Sciences (DIBINEM), University of Bologna, Bologna, Italy*
[b] *IRCCS Istituto delle Scienze Neurologiche di Bologna, Functional and Molecular Neuroimaging Unit, Bologna, Italy*
[c] *IRCCS Istituto delle Scienze Neurologiche di Bologna, Pituitary Unit, Bologna, Italy*
[d] *Department of Physics and Astronomy, University of Bologna, Bologna, Italy*
[e] *IRCCS Istituto delle Scienze Neurologiche di Bologna, Bologna, Italy*
[f] *Department for Life Quality Studies (QUVI), University of Bologna, Bologna, Italy*

ARTICLE INFO

ABSTRACT

The anterior optic pathway (AOP) is a system of three structures (optic nerves, optic chiasma, and optic tracts) that convey visual stimuli from the retina to the lateral geniculate nuclei. A successful reconstruction of the AOP using tractography could be helpful in several clinical scenarios, from presurgical planning and neuronavigation of sellar and parasellar surgery to monitoring the stage of fiber degeneration both in acute (e.g., traumatic optic neuropathy) or chronic conditions that affect AOP structures (e.g., amblyopia, glaucoma, demyelinating disorders or genetic optic nerve atrophies). However, its peculiar anatomy and course, as well as its surroundings, pose a serious challenge to obtaining successful tractographic reconstructions. Several AOP tractography strategies have been adopted but no standard procedure has been agreed upon.

We performed a systematic review of the literature according to the Preferred Reporting Items for Systematic Reviews and Meta-analyses (PRISMA) 2020 guidelines in order to find the combinations of acquisition and reconstruction parameters that have been performed previously and have provided the highest rate of successful reconstruction of the AOP, in order to promote their routine implementation in clinical practice. For this purpose, we reviewed data regarding how the process of anatomical validation of the tractographies was performed. The Cochrane Handbook for Systematic Reviews of Interventions was used to assess the risk of bias and thus the study quality We identified thirty-nine studies that met our inclusion criteria, and only five were considered at low risk of bias and achieved over 80% of successful reconstructions.

We found a high degree of heterogeneity in the acquisition and analysis parameters used to perform AOP tractography and different combinations of them can achieve satisfactory levels of anterior optic tractographic reconstruction both in real-life research and clinical scenarios. One thousand s/mm^2 was the most frequently used b value, while both deterministic and probabilistic tractography algorithms performed morphological reconstruction of the tract satisfactorily, although probabilistic algorithms estimated a more realistic percentage of crossing fibers (45.6%) in healthy subjects. A wide heterogeneity was also found regarding the method used to assess the anatomical fidelity of the AOP reconstructions. Three main strategies can be found: direct visual direct visual assessment of the tractography superimposed to a conventional MR image, surgical evaluation, and computational methods. Because the latter is less dependent on *a priori* knowledge of the anatomy by the operator, computational methods of validation of the anatomy should be considered whenever possible.

* Corresponding author.
  E-mail address: lauraludovica.gramegna@unibo.it (L.L. Gramegna).
[1] Contributed equally.

1. Introduction

The optic pathway is the system of anatomical structures that allows for vision by transmitting the light stimuli from the ocular globe to the occipital cortex of the brain (Stranding, 2020). It is divided into the anterior optic pathway (AOP), comprised of the optic nerve, optic chiasm, and optic tracts, and the posterior optic pathway. The optic nerve originates from the ganglion layer of the retina within the eye, which is located in the orbital cavity outside the skull, then enters the brain forming the optic chiasm and ends at the level of the lateral geniculate nucleus (LGN) in the thalamus, where a second neuron begins and extends to the primary visual cortex (V1 cortex) in the occipital lobe

forming the posterior optic pathway. The optic nerve within the orbit is surrounded by different tissues such as cerebrospinal fluid, the three meningeal layers (pia mater, arachnoid, dura mater), muscular and connective tissues of the extrinsic ocular muscles, fat, and air. After exiting the orbit, it forms the optic chiasm which is situated at the junction of the anterior wall and the floor of the third ventricle, approximately 5–10 mm above the hypophysis and the posterior part of the clinoid, a portion of the sphenoid bone composed of multiple pneumatic cells. After exiting the chiasm, the optic tracts contain the homolateral fibers of the same optic nerve and the contralateral crossing nerve fibers and originate from the posterolateral part of the optic chiasm (Stranding, 2020).
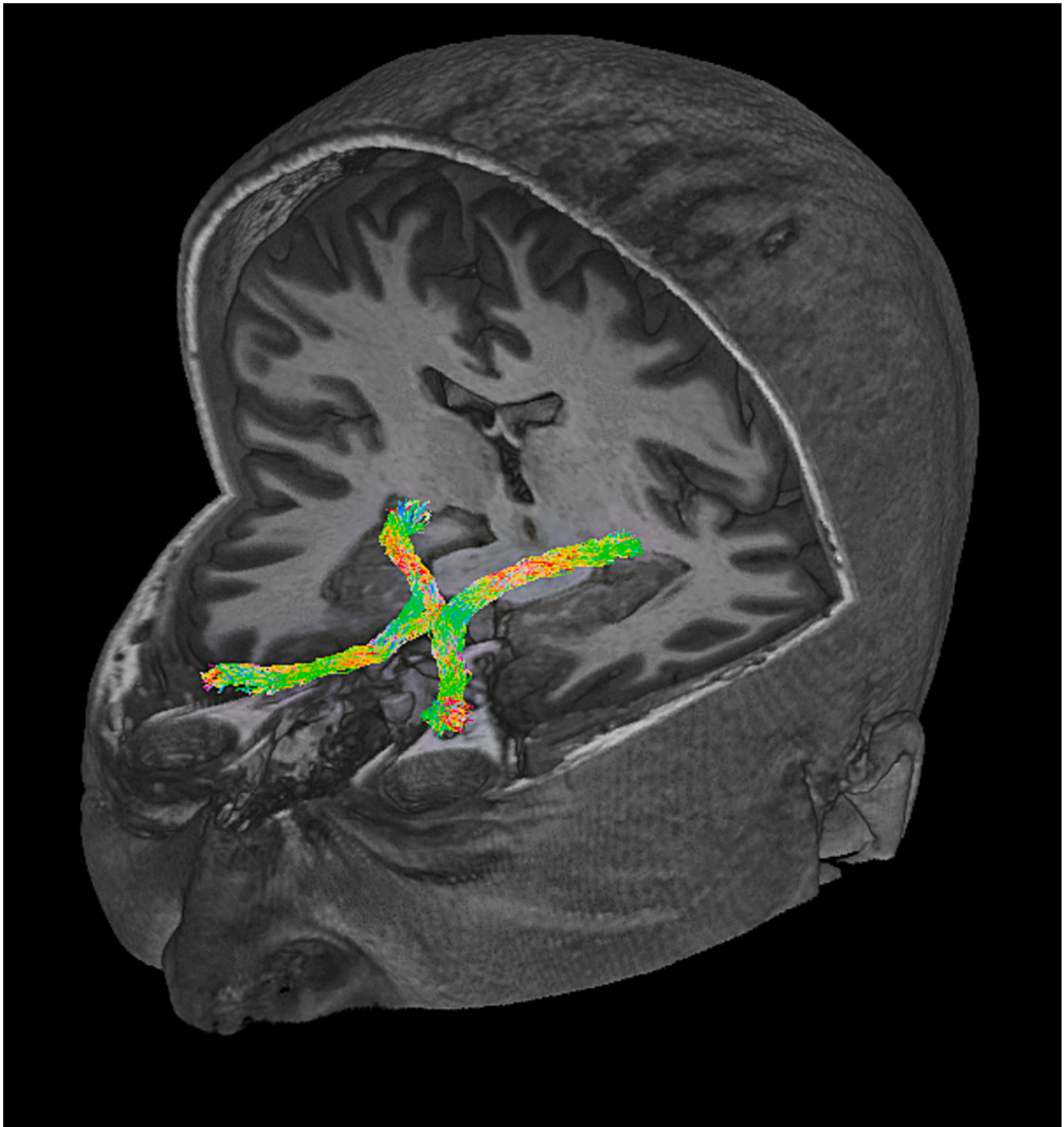

Fig. 1. Three-dimensional view of an AOP tractographic reconstruction superimposed to a 3D T1 MPRAGE image in a healthy adult obtained using a multishell CSD-based probabilistic tractography (iFOD1) pipeline.

Conventional Magnetic Resonance Imaging of cranial nerves is challenging, and the anterior optic pathway can be visualized by structural sequences only at high-resolution and under normal conditions, and it is difficult to trace in when in proximity with a sellar/parasellar tumor. Diffusion tensor imaging tractography is the only technique able to visualize the entire course of the anterior optic pathway in three-dimensions; it simultaneously permits the microstructural characterization of the AOP (Fig. 1).

The peculiar course of the AOP poses several challenges for the tractographical reconstruction. First, the intraorbital portion of the optic nerve is surrounded by different tissues, each presenting unique properties that contribute to an MRI signal characterized by partial voluming (i.e., voxels containing mixed information from multiple components) and magnetic susceptibility artifacts, both of which present challenges for nerve fiber tracking algorithms (He et al., 2021; Jacquesson et al., 2019b). In addition, the extraocular muscles also run mostly parallel to the optic nerve, and this can lead to false tracking of their fibers. Most importantly, a particular challenge of AOP tractography is the presence of fiber crossing in the optic chiasm. More specifically, the medial fibers (nasal fibers) cross the midline, while the lateral ones (temporal fibers) remain ipsilateral; and histologic studies report that around 56% of the fibers of the anterior optic pathway cross the midline (Chacko, 1948; Kupfer et al., 1967). This complex fiber geometry alters the shape of the diffusion signal decay in the voxels that correspond to fiber crossing and can lead to tracking errors if a tractography technique that is not capable of tracking multiple fiber orientations in the same voxel is employed.

The potential clinical utility of a tractographically defined anterior visual pathway has led several groups to face these technical challenges. For instance, it is of great interest among neurosurgeons dealing with neoplasms of the sellar and parasellar regions, (e.g., pituitary adenomas, tuberculum sellae meningiomas, craniopharyngiomas) that may cause extrinsic compression of the AOP fibers when extending superiorly (Ma et al., 2016) and for which surgical resection is challenging due to the high potential for damage to the visual system (Zoli et al., 2021). In fact, AOP tractography permits three-dimensional evaluation of the optic nerve, chiasma and tracts for surgical planning, potentially helping to reduce the risk of inadvertent damage during surgery. Further, it can be very useful in monitoring the stage of fiber degeneration in conditions such as multiple sclerosis (Reich et al., 2009), high tension glaucoma (Lestak et al., 2011), cones and rods dystrophy, and Leber's hereditary optic neuropathy (Ogawa et al., 2014; Takemura et al., 2019), or to assess conditions in which there is a deviation from normal anatomy at a microstructural level such as albinism (Ather et al., 2019; Puzniak et al., 2019) or amblyopia (Altıntaş et al., 2017) in the anterior optic pathway.

However, there is no accepted gold standard for the in vivo assessment of the anatomical fidelity of the tractography. Usually, direct visual assessment of the reconstructions is performed by the same operator who processed the tractographies even though this approach is highly susceptible to bias.

1.1. Aim

The goal of this study was to identify, through a systematic review of the literature, the combinations of acquisition and reconstruction diffusion imaging parameters that have been performed previously and have provided the highest rate of successful and *validated* reconstruction of the AOP in order to promote their routine implementation in clinical and research practice.

2. Material and methods

The study was conducted following the Preferred Reporting Items for Systematic Reviews and Meta-Analyses (PRISMA) guidelines (PROSPERO registration with the ID number CRD42022364565; https://www.crd.york.ac.uk/prospero/display_record.php?RecordID=364565) in order to find the combination of acquisition and analysis diffusion

imaging parameters that have achieved the highest level of anatomical fidelity of the reconstructions of the anterior optic pathway.

2.1. Inclusion and exclusion criteria

We included all studies conducted on humans, both healthy controls and patients with any disease, whose anterior visual pathway (including at least 2/3 of the structures between optic nerves, optic chiasm, optic tracts) was reconstructed in vivo using diffusion imaging tractography and the anatomical fidelity of the reconstruction was measured.

We excluded studies conducted on animals or on humans for whom different cranial nerves, white matter tracts or only one structure of the anterior visual pathway was reconstructed (i.e., only optic nerves, only optic chiasm, only optic tracts) as well as not providing any measure of the anatomical fidelity of the reconstructions.

2.2. Search strategy

A search was conducted in the MEDLINE/PubMed and Web of Science databases using the following search strategy: (((diffusion tensor imaging) OR (tractography)) AND (cranial nerve)) OR (((Optic nerve) OR (Optic pathways)) AND ((diffusion tensor imaging) OR (tractography))) retrieving only original articles and case reports written in English and published in international peer-reviewed journals from March 9th, 1999 up to June 15th, 2022.

2.3. Selection process

All the entries retrieved from the two web databases were processed independently by two authors (AC and LLG). First, preliminary sources were pooled and duplicates were removed. Then, the selection process was performed in two steps: first, by reading the articles' titles and abstracts to determine the presence of inclusion and absence of exclusion criteria. Entries that could not be immediately discarded were then read in their entirety to assess their eligibility.

2.4. Data extraction

All eligible entries were examined independently by two authors (AC and LLG) assessing the articles in their entire length as well as figures, tables, and supplementary materials provided by the authors. All the reported information regarding participants' conditions and demographics, diffusion imaging acquisition parameters, tractographic reconstruction process and its parameters, regions of interest (ROIs) used for seeding the fiber tracking, method used to assess the anatomical fidelity of the reconstructions and its results were noted on Microsoft Excel spreadsheets.

2.5. Data items

The main outcome of our study was the combination of acquisition and reconstruction diffusion imaging parameters with the highest rate of successful reconstruction of the AOP, considering successful a rate >80% according to the method used to assess the anatomical fidelity of the reconstructions.

Thus, all the available information on the following elements reported in plain text, figures, tables, and supplementary material of the selected entries were evaluated; number of subjects (patients and healthy controls are listed separately) and their demographics (age and sex); pathological condition (genetic conditions, ophthalmological diseases, space-occupying lesions, demyelinating disorders and other); diffusion imaging acquisition parameters (magnetic field strength, TR/TE, number of gradients, voxel size, b-value); tractographic reconstruction process and parameters (deterministic or probabilistic algorithm, fractional anisotropy (FA) / fiber orientation distribution (FOD) threshold, maximal curvature angle, minimal length, number of

generated streamlines, streamlines threshold number); ROIs used for seeding of the fiber tracking (number, their position, the role of the ROI, e.g., seed, waypoint, endpoint); method used to assess the anatomical fidelity of the reconstruction; results of the anatomical fidelity analysis (percentage of subjects in which the anterior optic pathway was successfully reconstructed) and method used to clear reconstructions from spurious fibers.

2.6. Risk of bias assessment

Risk of bias was evaluated following the Cochrane Handbook for Systematic Reviews of Interventions (Higgins et al., 2019). To avoid bias in the selection process, at least two authors independently performed each task. All the characteristics of the subjects, study design, and measures in every entry examined were carefully listed and checked to determine whether they could be tabulated with other entries or not.

In order to avoid systematic errors that could bias our results, we excluded all studies that did not report an assessment of the validation of the anatomical fidelity of the tractographic reconstructions. This was done because an assessment of anatomical fidelity is necessary to determine the kind and degree of bias risk inherent in a study.

We then classified studies into three categories of bias risk (low, medium and high) according to the method used to assess the anatomical fidelity of the reconstructions.

More specifically, studies that implemented only direct visual assessment of the reconstructions performed by the same operator who processed the tractographies were considered at high risk of bias. Studies were defined at medium risk of bias when the same process was performed by two or more different investigators. We defined at low risk of bias studies that implemented quantitative computational methods or surgical evaluation of the anatomical accuracy of tractographic reconstructions.

2.7. Effect measures

The main outcome measure was the result of anatomical fidelity analysis.

The method used for assessing the anatomical fidelity of the tractographic reconstructions was classified in three categories and annotated. The first is the direct visual assessment of the tractography superimposed onto a conventional morphological MR image: an expert visually inspected the MR images to define if the course of the reconstruction corresponded to the anatomy, with or without superimposing to a conventional MRI image (e.g., T1w, CISS). The second is the surgical evaluation: comparing the course of the pathway estimated using tractography to the one observed by a surgeon during a surgical operation. The last comprises the use of computational methods (i.e., quantitative measure of anatomical fidelity). An example is the computation of the percentage of crossing fibers reconstructed. Alternatively, the DICE co-efficient (Dice, 1945), a statistical tool which measures the similarity between two sets of data (X and Y), can be employed to measure the superimposition between images or volumes of the reconstruction using the equation $2\frac{|X \cap Y|}{|X+Y|}$. The Normalized Overlap Score (NOS) is one other example of method that can also be computed in order to quantify spatial agreement between two or more tractographic reconstructions. It is a quantitative measure of spatial agreement of a conjunction image generated by overlapping tractography masks. Given a conjunction image where its voxel value s denotes a range of overlap percentages between 0 and 100%, and value 1 denotes the 100% overlap value, this assumption can be formalized as $s \in [0,1]$, and NOS can be calculated using the following equation $n^{-1}\sum_{i=0}^{n-1}\frac{ln(\nu_1)}{ln(\nu_0)}$ where n was the number of bins; ν_0 was the number of voxels where $s > 0$; ν_i was the number of voxels with $0 < s \geq \frac{i}{n}$ (Chen et al., 2016). The LiFE (Pestilli et al., 2014) score given to each streamline together with the measure of distance between them and the tract core can be used, too.

2.8. Data synthesis methods

The rate of successful reconstruction, where reported, was calculated per structure (two per subject), counting each complete structure as successfully reconstructed based on the criteria of the individual report, converting counts from multiple structures (e.g., nerve chiasm, tract) based on the least successful subsegment, when these were the only values given. To allow for a fairer comparison of performance between studies evaluating different numbers of subjects, results were presented in graphical form using confidence intervals calculated based on the Wilson method (Agresti and Coull, 1998).

Given the large number of items recorded, data were tabulated thematically as follows: general study characteristics including study population, diffusion imaging parameters, tractography parameters, ROI selection methods, and results of tractography.

The success rate of reconstruction in the case of direct visual assessment was analysed graphically in order to investigate heterogeneity between studies. As participant counts were often low, confidence intervals were calculated for the fraction of successful reconstructions using the Wilson method. Studies reporting less than four cases were not included in the evaluation.

2.9. Harmonised scores

In order to facilitate comparison of visual assessment scores, a Harmonised Score (HS) was developed and these have been converted to a uniform scale (Table 5b-e) in which the lowest degree of success in reconstruction is represented by 0% and the highest by 100%.

3. Results

3.1. Study selection

Fig. 2 summarizes the selection process. A total of 1161 different entries were retrieved from the database search (n = 904 from MEDLINE/PubMed, n = 257 from Web of Science). After filtering based on article title and abstract, 89 were assessed in their entirety. Of these, 35 (Alshowaeir et al., 2014; Attyé et al., 2018; Backner et al., 2018; Burton et al., 2018; Cauquil et al., 2012; Dasenbrock et al., 2011; Frezzotti et al., 2016; Garaci et al., 2009; Garaci et al., 2008; Glick-Shames et al., 2019; Hana et al., 2014; Haykal et al., 2019; Haykal et al., 2020; Hoffmann et al., 2012; Hofstetter et al., 2019; Klistorner et al., 2014; Kolbe et al., 2012; Koller et al., 2019; Levin et al., 2010; Malania et al., 2017; Mascioli et al., 2012; Matsuo et al., 2018; Moon et al., 2021; Nucci et al., 2012; Ogawa et al., 2014; Raz et al., 2015a; Raz et al., 2015b; Raz and Levin, 2014; Roebroeck et al., 2008; Romero et al., 2012; Rutland et al., 2019; Schmidt et al., 2018; Stieglitz et al., 2011; Takemura et al., 2017; Touska and Connor, 2019; Yu et al., 2015) were excluded because only one out of three segments of the anterior optic pathway was reconstructed (e.g., only optic nerves, only optic chiasm, only optic tracts); 11 because they did not perform any form of assessment of anatomical fidelity of the reconstruction (Altobelli et al., 2015; Anik et al., 2011; Cauley and Filippi, 2013; Graham and Klistorner, 2017; Hales et al., 2018; Kuchling et al., 2017; Naismith et al., 2012; Paul et al., 2014; Purohit et al., 2016; Sims et al., 2021; Wang et al., 2011). One study was excluded because it was conducted ex vivo on anatomical dissection (Roebroeck et al., 2008). The remaining 39, published between 2007 and 2022, were included in the systematic review (Akazawa et al., 2010; Allen et al., 2018; Altıntaş et al., 2017; Ather et al., 2019; Chakravarthi et al., 2021; Davies-Thompson et al., 2013; de Blank et al., 2013; Ge et al., 2015; Hajiabadi et al., 2015; Hajiabadi et al., 2016; He et al., 2021; Ho et al., 2019; Hodaie et al., 2010; Hofer et al., 2010; Jacquesson et al., 2019a; Jin et al., 2019; Kamali et al., 2014; Kammen et al., 2016; Lacerda et al., 2021; Lecler et al., 2018; Liang et al., 2021; Lin et al., 2018; Lober et al., 2012; Ma et al., 2016; Maleki et al., 2012; Manners et al., 2022; Miller et al., 2019; Puzniak et al., 2019; Puzniak et al., 2021;
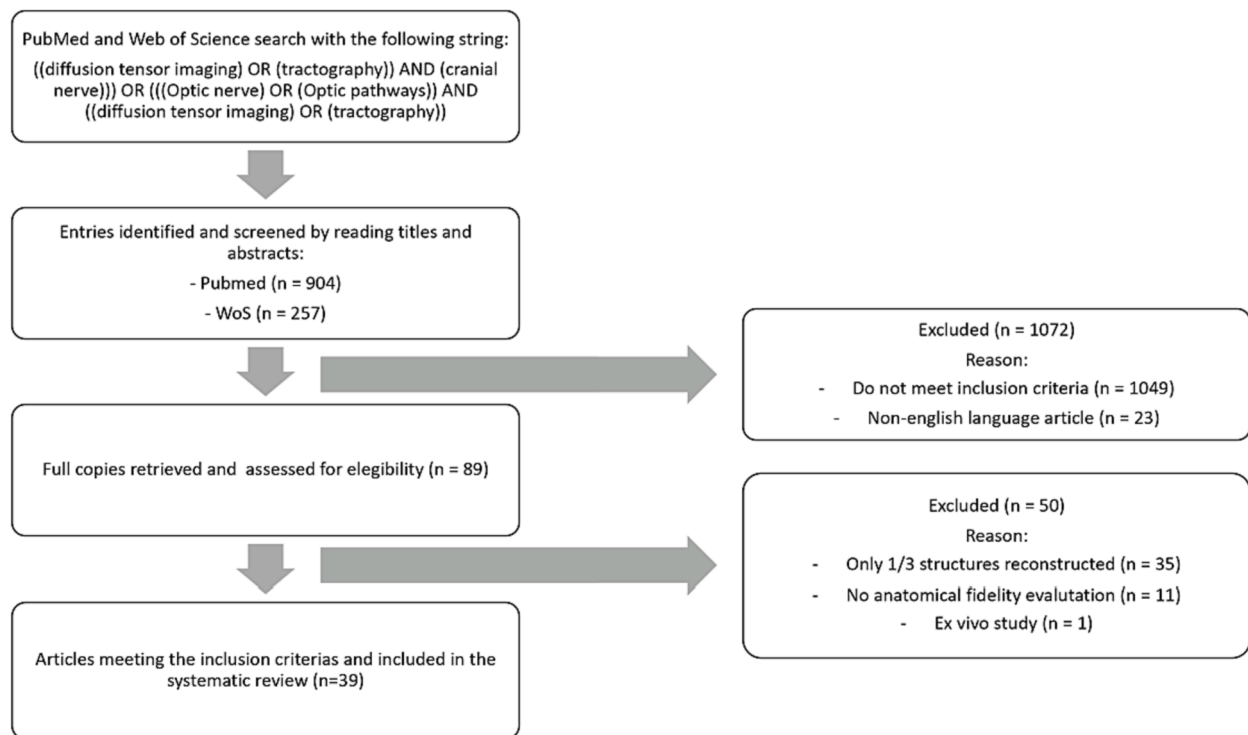
Fig. 2. Flowchart of systematic review and database returns. This figure graphically depicts the process of database search and review for article inclusion/exclusion.

Salmela et al., 2009; Staempfli et al., 2007; Takemura et al., 2019; Tao et al., 2009; Techavipoo et al., 2009; Wu et al., 2019; Yang et al., 2011; Yoshino et al., 2016; Zhang et al., 2012b; Zolal et al., 2017).

A total of 1530 different subjects were included, of whom 1100 (585 females) were healthy individuals and 438 (222 females) were affected by a pathological condition: 60 (12 females) had a genetic condition, 36 (10 females) had ophthalmological pathologies, 308 (187 females) space-occupying lesions, 16 (12 females) demyelinating disorders and the remaining 10 (1 female) other pathologies.

3.2. Characteristics of included studies

A summary of the principal characteristics of included studies can be found in Tables 1-5. Table 1 highlights the study populations.

Eight (20.5%) studies were conducted only on healthy volunteers (Akazawa et al., 2010; He et al., 2021; Hofer et al., 2010; Jin et al., 2019; Kamali et al., 2014; Kammen et al., 2016; Maleki et al., 2012; Staempfli et al., 2007), seven (17.9%) in patients affected by genetic conditions (e. g., albinism, congenital achiasma, Leber's hereditary optic neuropathy) (Ather et al., 2019; Davies-Thompson et al., 2013; Lecler et al., 2018; Manners et al., 2022; Puzniak et al., 2019; Puzniak et al., 2021; Takemura et al., 2019), three (7.7%) in patients affected by ophthalmological pathologies (e.g., amblyopia, aniridia, glaucoma) (Allen et al., 2018; Altıntaş et al., 2017; Miller et al., 2019), nineteen (48.7%) in patients with tumors or other expansive processes (de Blank et al., 2013; Ge et al., 2015; Hajiabadi et al., 2015; Hajiabadi et al., 2016; Ho et al., 2019; Hodaie et al., 2010; Jacquesson et al., 2019a; Liang et al., 2021; Lin et al., 2018; Lober et al., 2012; Ma et al., 2016; Salmela et al., 2009; Tao et al., 2009; Wu et al., 2019; Yoshino et al., 2016; Zhang et al., 2012b; Zolal et al., 2017), one (2.6%) in patients affected by demyelinating disorders (e.g., multiple sclerosis, neuromyelitis optica) (Techavipoo et al., 2009), and two (5.1 %) in patients with other pathologies (traumas, epilepsy) (Lacerda et al., 2021; Yang et al., 2011).

Twenty-eight studies (71.8%) performed tractography of the whole anterior optic pathway (Akazawa et al., 2010; Allen et al., 2018; Altıntaş et al., 2017; Ather et al., 2019; Chakravarthi et al., 2021; Davies-

Thompson et al., 2013; de Blank et al., 2013; Ge et al., 2015; He et al., 2021; Ho et al., 2019; Hodaie et al., 2010; Hofer et al., 2010; Jacquesson et al., 2019a; Kamali et al., 2014; Lacerda et al., 2021; Liang et al., 2021; Lin et al., 2018; Lober et al., 2012; Ma et al., 2016; Manners et al., 2022; Puzniak et al., 2019; Puzniak et al., 2021; Salmela et al., 2009; Staempfli et al., 2007; Tao et al., 2009; Yang et al., 2011; Yoshino et al., 2016; Zhang et al., 2012b), three (7.6%) reconstructed only the optic nerves and chiasm (Miller et al., 2019; Techavipoo et al., 2009; Zolal et al., 2017), two (5.1%) the optic nerves and tracts (Lecler et al., 2018; Wu et al., 2019), and the remaining six (15.4%) only the optic chiasm and tracts (Hajiabadi et al., 2015; Hajiabadi et al., 2016; Jin et al., 2019; Kammen et al., 2016; Maleki et al., 2012; Takemura et al., 2019).

3.3. Diffusion imaging acquisition parameters

Table 2 presents the main diffusion imaging acquisition parameters. Thirty-one studies (79.5%) were conducted using 3 T MRI (Allen et al., 2018; Altıntaş et al., 2017; Ather et al., 2019; Davies-Thompson et al., 2013; de Blank et al., 2013; Ge et al., 2015; He et al., 2021; Ho et al., 2019; Hodaie et al., 2010; Hofer et al., 2010; Jacquesson et al., 2019a; Jin et al., 2019; Kamali et al., 2014; Kammen et al., 2016; Liang et al., 2021; Lin et al., 2018; Lober et al., 2012; Ma et al., 2016; Maleki et al., 2012; Manners et al., 2022; Miller et al., 2019; Puzniak et al., 2019; Puzniak et al., 2021; Salmela et al., 2009; Staempfli et al., 2007; Takemura et al., 2019; Techavipoo et al., 2009; Wu et al., 2019; Yoshino et al., 2016; Zolal et al., 2017), seven (17,5%) at 1.5 T (Akazawa et al., 2010; Hajiabadi et al., 2015; Hajiabadi et al., 2016; Lacerda et al., 2021; Tao et al., 2009; Yang et al., 2011; Zhang et al., 2012b) and one (2.5%) used both 3 T and 1.5 T scanners (Chakravarthi et al., 2021). Repetition time (TR) and echo time (TE) ranged between 2300 and 17000 ms and 8.1–157 ms respectively. Voxel size ranged between 1.0 and 3.0 mm^3. The most common b value used was 1000 s/mm^2 (24/39, 61.5% entries) (Altıntaş et al., 2017; Ather et al., 2019; Chakravarthi et al., 2021; de Blank et al., 2013; Hajiabadi et al., 2016; He et al., 2021; Hodaie et al., 2010; Hofer et al., 2010; Jacquesson et al., 2019a; Jin et al., 2019; Kammen et al., 2016; Lacerda et al., 2021; Lin et al., 2018; Lober et al.,

Table 1
Summary of the general data of the included studies.

Article	Publication year	Disease class*	Condition	Patients/ healthy controls	Reconstructed segments			Magnetic Field (T)	Coil channels
					O.Nerves	Chiasma	O.Tracts		
J. He	2021	1	healthy controls	0/57	●	●	●	3	32
Z. Jin	2019	1	healthy controls	0/5		●	●	3	NA
A Kammen	2016	1	healthy controls	0/215		●	●	3	32
A. Kamali	2014	1	healthy controls	0/5	*	●	●	3	8
N. Maleki	2012	1	healthy controls	0/9		●	●	3	8
K Akazawa	2010	1	healthy controls	0/10	●	●	●	1.5	6
S Hofer	2010	1	healthy controls	0/6	●	●	●	3	32
P Staempfli	2007	1	healthy controls	0/10	●	●	●	3	8
D N Manners	2022	2	LHON	8/13	●	●	●	3	64
R Puzniak	2021	2	congenital achiasma albinism chiasmatic hypoplasia	11/8	*	●	*	3	64
S Ather	2019	2	albinism	23/20	●	●	●	3	32
R J Puzniak	2019	2	albinism	9/8	*	●	*	3	64
H Takemura	2019	2	LHON	7/20		●	●	3	12
A. Lecler	2018	2	congenital achiasma	1/0	●		●	NA	NA
J. Davies-Thompson	2013	2	congenital achiasma	1/9	●	●	●	3	NA
N. Miller	2019	3	glaucoma	6/6	●	●		3	32
B. Allen	2018	3	amblyopia	15/13	●	●	●	3	32
Ö Altıntaş	2017	3	amblyopia	15/10	●	●	●	3	8
S S Chakravarthi	2021	4	skull base meningiomas	24/0	●	●	●	3 1.5	8 8
L Liang	2021	4	hypophiseal macroadenoma	65/33	●	●	●	3	64
C Y Ho	2019	4	OPG	12/12	●	●	●	3	NA
T. Jacquesson	2019	4	skull base tumors	5/0	●	●	●	3	32
C N Wu	2019	4	orbital space occupying lesions	20/25	●		●	3	8
J Lin	2018	4	sellar region tumors	2/0	●	●	●	3	NA
J. Ma	2017	4	meningioma hypofiseal adenoma	5/0	●	●	●	3	8
A Zolal	2017	4	meningioma	2/30	●	●		3	NA
M. Yoshino	2016	4	brain tumors	3/488	●	●	●	3	32
M Haijabadi	2016	4	suprasellar tumors compressing the chiasma	25/6		●	●	1.5	NA
M. Ge	2015	4	OPG	11/0	●	●	●	3	8
M. Hajiabadi	2015	4	hypophiseal macroadenoma together with glaucoma or GCA	2/0		●	●	1.5	NA
P. M. K. De Blank	2013	4	OPG NF1 type	50/0	●	●	●	3	NA
R. M. Lober	2012	4	OPG	10/0	●	●	●	3	8
Y Zhang	2012	4	orbital tumors occipital lobe tumors	36/30	●	●	●	1.5	8
M. Hodaie	2010	4	CNS tumors	4/0	●	●	●	3	8
M B Salmela	2009	4	pediatric suprasellar tumors	2/10	●	●	●	3	8
X-F Tao	2009	4	orbital tumors orbital chronic inflammation	30/15	●	●	●	1.5	8
U Techavipoo	2009	5	multiple sclerosis	16/7	●	●		3	8
L M Lacerda	2021	6	epilepsy	4/20	●	●	●	1.5	NA
Q T Yang	2011	6	traumatic optic neuropathy	6/0	●	●	●	1.5	8

Disease class: 1 healthy subjects only, 2 genetic conditions, 3 ophthalmological disorders, 4 space-occupying lesions, 5 demyelinating disorders, 6 other pathologies. * = partial reconstruction of the segment.

Abbreviations: GCA - giant cell arteritis; OPG - optic pathway glioma; NF1 – neurofibromatosis type 1; LHON - Leber's hereditary optic neuropathy; NA – not assessed; CNS - central nervous system.

2012; Ma et al., 2016; Maleki et al., 2012; Manners et al., 2022; Salmela et al., 2009; Staempfli et al., 2007; Takemura et al., 2019; Tao et al., 2009; Wu et al., 2019; Yang et al., 2011; Zhang et al., 2012b), with 5000 s/mm^2 being the maximum used (Yoshino et al., 2016). Five entries (12.1%) performed multishell diffusion imaging (He et al., 2021; Kammen et al., 2016; Liang et al., 2021; Manners et al., 2022; Yoshino et al., 2016). The number of directions ranged between 6 and 270 with 32 being the most frequently used (6/39, 15.4%) (Akazawa et al., 2010; Davies-Thompson et al., 2013; Jacquesson et al., 2019a; Lin et al., 2018; Ma et al., 2016; Techavipoo et al., 2009). Six entries (15.4%) can be classified as HARDI (Ather et al., 2019; He et al., 2021; Kammen et al., 2016; Liang et al., 2021; Manners et al., 2022; Puzniak et al., 2019; Puzniak et al., 2021; Yoshino et al., 2016). The average scan time was 10.3 ± 4.7 min (range, 3 – 22.4 min) with sixteen entries (41%) adopting an accelerating technique (Ather et al., 2019; Chakravarthi et al., 2021; Davies-Thompson et al., 2013; He et al., 2021; Hofer et al., 2010; Kamali et al., 2014; Kammen et al., 2016; Liang et al., 2021; Lober

et al., 2012; Maleki et al., 2012; Manners et al., 2022; Staempfli et al., 2007; Takemura et al., 2019; Techavipoo et al., 2009; Yoshino et al., 2016; Zhang et al., 2012b).

3.4. Tractographic reconstruction parameters

Table 3 presents the main tractographic reconstruction parameters. Regarding signal modeling, twenty-four studies (61.5%) used only the standard diffusion tensor (DT) model (Akazawa et al., 2010; Altıntaş et al., 2017; Ather et al., 2019; Chakravarthi et al., 2021; Davies-Thompson et al., 2013; de Blank et al., 2013; Ge et al., 2015; Hajiabadi et al., 2015; Hajiabadi et al., 2016; Hodaie et al., 2010; Hofer et al., 2010; Kamali et al., 2014; Lin et al., 2018; Lober et al., 2012; Ma et al., 2016; Maleki et al., 2012; Salmela et al., 2009; Staempfli et al., 2007; Takemura et al., 2019; Tao et al., 2009; Techavipoo et al., 2009; Wu et al., 2019; Yang et al., 2011; Zhang et al., 2012b), seven (17.9%) only constrained spherical deconvolution (CSD) (Allen et al., 2018;

Table 2
Summary of diffusion image acquisition parameters of studies included.

Article	TR/TE (ms)	Voxel size (mm^3)	b-values	b [min – max] (s/mm^2)	Gradient directions	AP/PA phase encoding	Acceleration factor	Scan time	HARDI	Multishell
He (2021)	5520/89,5	1.25x1.25x1.25	3	1000——3000	270	Yes*	3	9 min 50 s	yes	Yes+
Jin (2019)	8000/108	1x1x2.4	1	1000	25	no	no	3 min 36 s	no	no
Kammen (2016)	5520/89,5	1.25x1.25x1.25	3	1000——3000	270	Yes*	3	9 min 50 s	yes	yes
Kamali (2014)	14460/60	2.29x2.29x1	1	500	NA	no	SENSE 2	7 min◆	no	no
Maleki (2012)	7900/92	1.75x1.75x2.5	1	1000	NA	no	three fold SENSE	10 min	no	no
Akazawa (2010)	5000/55, 65, 72, 78	3.0x3.0x3.0	4	700——2800	32	no	no	6 min♠	no	no
Hofer (2010)	NA/NA	1.8x1.8x1.8	1	1000	24	no	2	5 min	no	no
Staempfli (2007)	NA/45,8	1.719x1.718x1.8	1	1000	15	no	SENSE 5	NA	no	no
Manners (2022)	4300/98	2x2x2	3	300——2000	113	yes	in plane = 2 multiband = 3	9 min	yes	yes
Puzniak (2021)	9400/64	1.5x1.5x1.5	1	1600	128	yes	no	NA	yes	no
Ather (2019)	8270/67	1.8x1.8x1.8	1	1000	61	no	SENSE 3	9 min 30 s	yes	no
J Puzniak (2019)	9400/64	1.5x1.5x1.5	1	1600	128	yes	no	22 min 24 s	yes	no
Takemura (2019)	7500/93	1.8x1.8x1.8	1	1000	12	no	2	10 min 30 s	no	no
Lecler (2018)	NA/NA	NA	NA	NA	NA	NA	NA	NA	NA	NA
Davies-Thompson (2013)	5486/69	2.21x2.21x2.2	1	700	32	no	SENSE	NA	no	no
Miller (2019)	8100/76,7	2x2x2	1	2000	48	yes	no	15 min	no	no
Allen (2018)	8100/76,7	2x2x2	1	2000	48	yes	no	NA	no	no
Altıntaş (2017)	4805/59	2x2x2	1	1000	15	no	no	6 min 5 s	no	no
Chakravarthi (2021)	17000/80,8	2x2x2.6	1	1000	24	no	NEX 1	NA	no	no
Liang (2021)	7700/79	2.2x2.2x2.2	19	200——3000	128	no	2	18 min	yes	yes
Ho (2019)	ssDTI: 4200–2500/ 152–86 rsDTI: 2800–2300/ 70–68	1.3x1.3x2.2	3	250 – 800	12	no	no	12 min 19 s 12 min 10 s	no	no
Jacquesson (2019)	3956/102	2x2x2	1	1000	32	yes	no	9 min 52 s	no	no
Wu (2019)	8300/91	2.0x2.0x2.0	1	1000	NA	no	no	12 min 4 s	no	no
Lin (2018)	7849/80	1x1x1	1	1000	32	no	no	NA	no	no
Ma (2017)	NA/NA	1.6x1.6x2	1	1000	32	no	no	NA	no	no
Zolal (2017)	NA/NA	2x2x2	1	800	20	no	no	NA	no	no
Yoshino (2016)	9916/157	2.4x2.4x2.4	14	384——5000	101	no	3	15 min	yes	yes
Haijabadi (2016)	NA/NA	1.875x1.875x9	1	1000	20	no	no	NA	no	no
Ge (2015)	11000/94	2.0x2.0x2.0	NA	NA	30	no	no	6 min 16 s	no	no
Hajiabadi (2015)	NA/NA	1.875x1.875x1.9	NA	NA	20	no	no	NA	no	no
De Blank (2013)	7300–11600/ 91–93 9400–9600/84 9400–14000/ 91–104	2x2x2 2x2x2.5	1	1000	20 20–30	no	no	NA	no	no
Lober (2012)	NA/NA	NA	1	1000	25	no	3	NA	no	no
Zhang (2012)	6000/60,1	1.875x1.875x3.5	1	1000	13	no	NEX 2	NA	no	no
Hodaie (2010)	12000/86.6	3.0x3.0x3.0	1	1000	25	no	no	NA	no	no
Salmela (2009)	7623/57	1.9x2x2	1	1000	6	no	no	3 min 58 s	no	no
Tao (2009)	4500/73	1.875x1.846x2	1	1000	25	no	no	14 min 30 s	no	no
Techavipoo (2009)	7000/92	1.5x1.5x3	1	850	32	no	SENSE 2,5	9 min	no	no
Lacerda (2021)	6300/89	2.5x2.5x2.5	1	1000	20	no	no	NA	no	no
Yang (2011)	6000/60,1	1.875x1.875x2	1	1000	13	no	no	17 min	no	no

Abbreviations: NA – not assessed; SENSE - sensitivity encoding; NEX – number of excitations; ssDTI - single-shot echo planar imaging DTI; rsDTI - readout-segmented multi-shot DTI.

Legend: * = Opposite phase encoding directions on the latero-lateral plane (left–right and right left); + = Multishell DTI acquisition, but only a single shell (b = 1000 s/mm^2) processed for tractography; ◆ = DTI acquisition was repeated three times (total acquisition 21 min); ♠ = Multiple single-shell acquisitions with different b values. Scan time for a single b value (total acquisition 24 min).

Jacquesson et al., 2019a; Kammen et al., 2016; Lacerda et al., 2021; Lecler et al., 2018; Manners et al., 2022; Miller et al., 2019), three (7.7%) only generalized q-sampling imaging (GQI) (Ho et al., 2019; Liang et al., 2021; Yoshino et al., 2016), three (7.7%) both DT and CSD (He et al., 2021; Puzniak et al., 2019; Puzniak et al., 2021), one (2.6%) DT and GQI (Jin et al., 2019), and one (2.6%) GQI and CSD (Zolal et al., 2017).

Regarding the tractography reconstruction algorithm, twenty-three studies (60%) used a deterministic algorithm to generate tractographies (Akazawa et al., 2010; Altıntaş et al., 2017; Chakravarthi et al., 2021; de Blank et al., 2013; Ge et al., 2015; Hajiabadi et al., 2015; Hajiabadi et al., 2016; Ho et al., 2019; Hodaie et al., 2010; Hofer et al., 2010; Jin et al., 2019; Kamali et al., 2014; Liang et al., 2021; Lin et al., 2018; Lober et al., 2012; Ma et al., 2016; Salmela et al., 2009; Staempfli et al., 2007; Tao et al., 2009; Techavipoo et al., 2009; Yang et al., 2011; Yoshino et al., 2016; Zhang et al., 2012b), and thirteen (32.5%) a probabilistic method (Allen et al., 2018; Ather et al., 2019; Davies-Thompson et al., 2013; Jacquesson et al., 2019a; Kammen et al., 2016; Lacerda et al., 2021; Lecler et al., 2018; Maleki et al., 2012; Manners et al., 2022; Miller et al., 2019; Takemura et al., 2019; Wu et al., 2019). Four studies (10%) performed both types of tractography (He et al., 2021; Puzniak et al., 2019; Puzniak et al., 2021; Zolal et al., 2017).

For deterministic tractography, the most frequently used cut-off FA/FOD amplitude value (depending on the tractography algorithm used) was 0.15 (4/28; 14,3%) (de Blank et al., 2013; Hajiabadi et al., 2015; Salmela et al., 2009; Tao et al., 2009) with values ranging between 0.004 and 0.5. The angular threshold was set to between 5° and 80° with 60° being the most used (4/28; 14.3%) (Ho et al., 2019; Kamali et al., 2014; Puzniak et al., 2019; Yoshino et al., 2016). Step size was set to between 0.15 mm and 1.2 mm with 1.2 mm being the most commonly used (3/28; 10.7%) (Jin et al., 2019; Liang et al., 2021; Yoshino et al., 2016).

For probabilistic tractography, the FA/FOD amplitude cut off most often used (depending on the tractography algorithm used) was 0.005 (2/17; 11.8%) (He et al., 2021; Manners et al., 2022) with values ranging between 0.005 and 0.5. The angular threshold was set to between 2° and 90° with 11° being the most used (4/17; 23,5%) (Ather et al., 2019; Davies-Thompson et al., 2013; Maleki et al., 2012; Wu et al., 2019). Step size was set to between 0.15 mm and 2 mm with 0.5 mm being the most commonly selected (3/17; 17.6%) (Ather et al., 2019; Davies-Thompson et al., 2013; Maleki et al., 2012).

3.5. Regions of interest selection

The selection of ROIs reported in the literature can be found in Table 4.

The most common areas selected as ROIs are the orbital optic nerve (12/40, 30%) (Allen et al., 2018; Altıntaş et al., 2017; Hales et al., 2018; He et al., 2021; Liang et al., 2021; Ma et al., 2016; Manners et al., 2022; Miller et al., 2019; Salmela et al., 2009; Staempfli et al., 2007; Yoshino et al., 2016; Zolal et al., 2017), the chiasm (29/40, 72,5%) (Allen et al., 2018; Altıntaş et al., 2017; Ather et al., 2019; de Blank et al., 2013; Ge et al., 2015; Hajiabadi et al., 2015; Hajiabadi et al., 2016; Hales et al., 2018; He et al., 2021; Ho et al., 2019; Hofer et al., 2010; Jacquesson et al., 2019a; Jin et al., 2019; Kamali et al., 2014; Kammen et al., 2016; Lacerda et al., 2021; Lober et al., 2012; Maleki et al., 2012; Manners et al., 2022; Miller et al., 2019; Salmela et al., 2009; Staempfli et al., 2007; Takemura et al., 2019; Tao et al., 2009; Techavipoo et al., 2009; Yang et al., 2011; Zhang et al., 2012b; Zolal et al., 2017), and the LGN (14/40, 35%) (Allen et al., 2018; Altıntaş et al., 2017; de Blank et al., 2013; Hales et al., 2018; He et al., 2021; Hodaie et al., 2010; Hofer et al.,

2010; Jin et al., 2019; Lacerda et al., 2021; Liang et al., 2021; Maleki et al., 2012; Manners et al., 2022; Takemura et al., 2019; Yoshino et al., 2016). The ROIs selection process is usually done manually at the single subject level, with an expert manually drawing them over the selected structures. T1-weighted were the most popular images used for this process (21/40, 52,5%) (Allen et al., 2018; Altıntaş et al., 2017; Davies-Thompson et al., 2013; Ge et al., 2015; Hajiabadi et al., 2015; Hodaie et al., 2010; Hofer et al., 2010; Jin et al., 2019; Kammen et al., 2016; Lacerda et al., 2021; Ma et al., 2016; Maleki et al., 2012; Miller et al., 2019; Puzniak et al., 2019; Puzniak et al., 2021; Staempfli et al., 2007; Takemura et al., 2017; Tao et al., 2009; Wu et al., 2019; Yoshino et al., 2016; Zolal et al., 2017). Alternatives included Constructive Interference in Steady State (CISS) / Fast Imaging Employing Steady-state Acquisition (FIESTA) images (3/40, 7,5%) (Jacquesson et al., 2019a; Ma et al., 2016; Zolal et al., 2017), FA Direction Encoding Color (DEC) map (4/40, 10%) (Hales et al., 2018; He et al., 2021; Kamali et al., 2014; Zhang et al., 2012b), FA map (3/40, 7,5%) (Ather et al., 2019; Ho et al., 2019; Liang et al., 2021), and EPI images without diffusion weighting (Akazawa et al., 2010; de Blank et al., 2013; Salmela et al., 2009). Four studies presented an automatic method of ROI selection using MNI standard space aligned to the diffusion-weighted space as reference (Manners et al., 2022), averages of ROIs defined on a small subsample of the study population (Kammen et al., 2016) or segmentations of the T1w images using FreeSurfer software and Juelich histological atlas (Kammen et al., 2016; Maleki et al., 2012).

3.6. Method used to assess the anatomical fidelity of the reconstruction

Table 7 summarizes the anatomical fidelity evaluations performed in the studies included in the review. Given the wide variety of evaluation methods, results are divided into 5 parts, covering direct visual assessment (simple success/fail, with fractional score divided by eye or by segment), visual assessment score, surgical evaluation, percentage of fiber crossings reconstructed, and other evaluation methods (mainly DICE score or NOS score). For each study, results are further divided vertically when multiple evaluations were performed to compare methods or time points, and horizontally to divide healthy control and patient populations.

Table 5 shows a complete summary of the anatomical fidelity assessment of the reconstruction, grouped by assessment method.

Direct visual assessment was used in thirty-five studies (Akazawa et al., 2010; Allen et al., 2018; Altıntaş et al., 2017; Davies-Thompson et al., 2013; de Blank et al., 2013; Ge et al., 2015; Hajiabadi et al., 2015; Hajiabadi et al., 2016; He et al., 2021; Ho et al., 2019; Hodaie et al., 2010; Hofer et al., 2010; Jacquesson et al., 2019a; Jin et al., 2019; Kamali et al., 2014; Kammen et al., 2016; Lacerda et al., 2021; Lecler et al., 2018; Liang et al., 2021; Lin et al., 2018; Lober et al., 2012; Ma et al., 2016; Maleki et al., 2012; Manners et al., 2022; Miller et al., 2019; Salmela et al., 2009; Staempfli et al., 2007; Takemura et al., 2019; Tao et al., 2009; Techavipoo et al., 2009; Wu et al., 2019; Yang et al., 2011; Yoshino et al., 2016; Zhang et al., 2012b; Zolal et al., 2017). Among these, nineteen reported 100% successful reconstructions (Allen et al., 2018; Altıntaş et al., 2017; Davies-Thompson et al., 2013; Hodaie et al., 2010; Jacquesson et al., 2019a; Kamali et al., 2014; Kammen et al., 2016; Lacerda et al., 2021; Lecler et al., 2018; Liang et al., 2021; Ma et al., 2016; Maleki et al., 2012; Miller et al., 2019; Staempfli et al., 2007; Takemura et al., 2019; Techavipoo et al., 2009; Wu et al., 2019; Yoshino et al., 2016; Zhang et al., 2012b), three reported between 90 and 100% (de Blank et al., 2013; Ho et al., 2019; Lober et al., 2012), four studies between 80 and 90% successful reconstructions (Hofer et al., 2010; Lin et al., 2018; Manners et al., 2022; Tao et al., 2009), and nine under 80% successful reconstructions (Akazawa et al., 2010; Ge et al.,

Table 3
Summary of the tractographic analysis parameters of the included studies.

Article	Signal modeling	Deterministic	Probabilistic	FA or other threshold	Max curvature	Steps (mm)	Streamline generation	Other (e.g., filtering)
He (2021)	DTI; CSD	SD-Stream, UKF-1 T, UKF-2 T	iFOD1	seed = 0.006; stop = 0.005 (SD-Stream. iFOD1) seed = 0.02; stop = 0.01 (UKFs)	SD-Stream: 80° iFOD-1: 10°	NA	40,000 fibers generated for each method	Fiber threshold length = 45 mm
Jin (2019)	DTI; GQI	DSI-Studio TRACKVIS	no	0.04	50°	1.2	1500 fibers reconstructed	
Kammen (2016)	CSD	No	ConTrack	NA	2 mm	NA	1000 streamlines generated	
Kamali (2014)	DTI	DTI-Studio software FACT	no	0.22	60°	NA		Spurious fiber cleaning with ROEs (see Table 4)
Maleki (2012)	DTI	No	FSL 4.1.3	0.2	0.2	0.5	25,000 streamlines generated	
Akazawa (2010)	DTI	PRIDE software (2 tensor model)	no	Principal diffusivities (λ_1, λ_2, and λ_3) were restricted respectively to range 1.2–1.8, 0.2–0.7, and 0.2–0.7 (10^{-3} mm^2/s), to capture highly oriented fibers	NA	NA		
Hofer (2010)	DTI	Tensorline	no	0.1	70°	NA		
Staempfli (2007)	DTI	aFM	no	NA	NA	NA	60,000 to 65,000 time steps	8 to 12% voxel connectivity
Manners (2022)	CSD	No	iFOD1	seed = 0.006; stop = 0.005	10°	NA		
Puzniak (2021)	DTI; CSD	DT based, CSD based	iFOD2	NA	5°, 10°, 20°, 40°, 80°	0.15; 0.75	15,000 streamlines generated	Minimum length 7.5 mm; LiFE method for filtering spurious streamlines
Ather (2019)	DTI	No	PROBTRACKX2	0.1	0.2 mm	0.5	5000 streamlines generated; two reconstructions (seed and target reversed) averaged together	
J Puzniak (2019)	DTI; CSD	DT Tensor Prob	iFOD2	DT Tensor Prob: 0.04; 0.08. iFOD2: 0.04; 0.08	30°; 45°; 60°	NA	139,000 streamlines generated.	Different spurious streamline filtering strategies (LIFE, COMMIT-SZB, COMMIT-SB, SIFT2) max streamline length 80 mm
Takemura (2019)	DTI	No	ConTrack	NA	90°	1	5000 streamlines generated. Only 1000 retained; two runs were performed on different DTI acquisitions and merged together	
Lecler (2018)	CSD	no	CSD based	NA	NA	NA		
Davies-Thompson (2013)	DTI	No	FSL Probtrackx	NA	0.2	0.5	5000 streamlines generated	
Miller (2019)	CSD	no	Mrtrix 2 CSD based	NA	NA	NA	5,000,000 fibers generated	AFQ toolkit used to remove fibers 2.6 sd distance away from the fiber core. Further manual cleaning (superimposed on T1w) manual spurious fiber cleaning
Allen (2018)	CSD	no	Mrtrix CSD-based	0.2	60°	2		
Altıntaş (2017)	DTI	FACT	no	NA	NA	NA		
Chakravarthi (2021)	DTI	BrightMatter Plan software	no	NA	NA	NA	whole brain tractography that also reconstructed the whole anterior visual pathway	
Liang (2021)	GQI	DSI-Studio software	no	0.20–0.35	70°	1.2		minimum length 10 mm; maximum length 300 mm
Ho (2019)	GQI	DSI-Studio software	no	NA	60°	0.6	10,000 fibers generated	minimum length 30 mm
Jacquesson (2019)	CSD	no	Mrtrix 3 "tckgen"	0.3	45°	1	1000 fibers generated	Spurious fiber cleaning with ROEs (see Table 4)
Wu (2019)	DTI	No	PROBTRACKX	NA	0.2	NA	5000 streamlines generated	10% threshold
Lin (2018)	DTI	Mimics research 17.0 software	no	NA	NA	NA		

Table 3 (*continued*)

Article	Signal modeling	Deterministic	Probabilistic	FA or other threshold	Max curvature	Steps (mm)	Streamline generation	Other (e.g., filtering)
Ma (2017)	DTI	3D Slicer software	no	0.18	0.7	0.5		Path length between 20 and 800
Zolal (2017)	CSD; GQI	DSI-Studio software	FSL 5.0	0.5	80°	0.4		For probabilistic tractography PICo maps were created. To find the optimal probability threshold for localizing the nerve, the resulting PICo maps were filtered at threshold values of 0.05–0.95 in steps of 0.05
Yoshino (2016)	GQI	DSI-Studio	no	0.02–0.5	60-70°	1.2	1000 to 10 000 streamlines generated	To smooth each tract, the next directional estimate of each voxel was weighted by 20% of the previous moving direction and by 80% of the incoming direction of the fiber
Haijabadi (2016)	DTI	BrainLAB workstation	no	0.01	NA	NA		Minimum fiber length 5 mm
Ge (2015)	DTI	Neuro 3D software	no	0.05	30°	NA		
Hajiabadi (2015)	DTI	BrainLAB workstation	no	0.15	NA	NA		minimum fiber length: 21 mm
De Blank (2013)	DTI	DTI-Studio software FACT	no	0.15	70°	NA		
Lober (2012)	DTI	InVivo Dynasuite software	no	0.05	30°	NA		
Zhang (2012)	DTI	dTV 1.72 software	no	0.2	NA	NA		
Hodaie (2010)	DTI	3D Slicer software	no	0.2	0.8	0.5		Manual fiber cleaning using "ROI select NOT" operation on spurious fibers
Salmela (2009)	DTI	FACT	no	0.15	27	NA		Minimum fiber length 10 mm
Tao (2009)	DTI	dTV 2.0 software	no	0.15	NA	<200		
Techavipoo (2009)	DTI	FACT	no	0.25	80°	0.8		
Lacerda (2021)	CSD	No	MRTrix, CSD based	NA	NA	NA		based on command 3Tissue to extract CSD
Yang (2011)	DTI	dTV 2.0, Volume One 1.72 software	no	NA	NA	NA		

Abbreviations: DT – diffusion tensor; UKF - unscented Kalman filter; CSD – constrained spherical deconvolution; LiFE – linear fascicle evaluation; COMMIT - convex optimization modeling for microstructure informed tractography; SIFT - spherical-deconvolution informed filtering of tractograms; FACT – fiber assignment by continuous tracking; ROI – region of interest; PICo - probabilistic index of connectivity; NA – not assessed, aFM - advanced fast marching algorithm; FOD - fiber orientation density.

2015; Hajiabadi et al., 2015; Hajiabadi et al., 2016; He et al., 2021; Jin et al., 2019; Salmela et al., 2009; Yang et al., 2011; Zolal et al., 2017).

Harmonised scores (HS) are available Table 5b-e.

Assessment through the surgical endoscope was performed in five studies (Chakravarthi et al., 2021; Ge et al., 2015; Jacquesson et al., 2019a; Ma et al., 2016; Zolal et al., 2017). Among these, four achieved 100% of successful reconstruction, while one 50% (Zolal et al., 2017).

Six studies (15%) implemented a computational approach to test the anatomical fidelity of the reconstructions. Four reported the percentage of the crossing fibers reconstructed: 49.1% (Manners et al., 2022); 45.4% (He et al., 2021); 35.8% (Ather et al., 2019); and 30.2% (Puzniak et al., 2019). Considering this metric, reconstructions are considered successful if this percentage is close to the 50% value, which is considered a good approximation of the results of histological dissection studies (Chacko, 1948; Kupfer et al., 1967).

Three studies implemented the DICE coefficient to measure superimposition between a segmentation of the pathway extracted from a T1w image, crossing and non-crossing fibers (Manners et al., 2022), volume of the anterior optic pathway calculated from the reconstructions and T1w-based segmentations generated from a mask drawn over the MNI atlas (He et al., 2021). The results achieved were 49.5% and 73.8%, respectively.

In one study (He et al., 2021) the spatial superimposition between the reconstructions was measured by computing the NOS score. The average result is 0.557.

Another study (Puzniak et al., 2019) evaluated the reconstructions using the Linear Fascicle Evaluation (LiFE) method. The dispersion of the reconstructed streamlines around the tract core was also measured.

In 7/40 studies (17.5%) (Allen et al., 2018; He et al., 2021; Jacquesson et al., 2019a; Kamali et al., 2014; Miller et al., 2019; Puzniak et al., 2019; Puzniak et al., 2021) a specific step regarding spurious fiber cleaning was included in the processing pipeline.

This process was done manually after direct visual inspection in two entries (Allen et al., 2018; Miller et al., 2019), two of them using region of exclusions (ROEs) to perform this task (Jacquesson et al., 2019a; Kamali et al., 2014), while two used a filtering algorithm (Puzniak et al., 2019; Puzniak et al., 2021) and one also used a specific fiber cleaning tool (AFQ toolkit) (Miller et al., 2019).

Table 4
Summary of the ROI selection process of included articles.

Article	Sequence used as reference	Anatomic regions
He (2021)	DEC map	Orbit (seed), Chiasm (waypoint), LGN (target)
Jin (2019)	3D T1w	Optic chiasm (seed), LGN (target)
Kammen (2016)	3D-MPRAGE T1w	Chiasm (automatically defined by creating an average of 5 subjects - seed), LGN (FSL distance function between thalamus and hippocampus - target)
Kamali (2014)	DEC map	Chiasm (seed), Fiber AP oriented passing through the anterior commissure (target), Optic nerve (at the level of the rostrum of the corpus callosum - target), Thalamic fibers that loop around the temporal horn of the lateral ventriculus (ROE), AP oriented fibers in the occipital cortex (ROE)
Maleki (2012)	3D-MPRAGE T1w using FreeSurfer Juelich histological atlas	Optic chiasm (seed), LGN (target)
Akazawa (2010)	B0 image	Optic nerve (seed), Optic tract (target)
Hofer (2010)	3D FLASH T1w	Chiasm (seed), LGN (target)
Staempfli (2007)	T1w TFE	Orbit (seed), Chiasm (seed)
Manners (2022)	MNI atlas	Orbit (target), Chiasm (waypoint), LGN (seed)
Puzniak (2021)	3D-MPRAGE T1w	Optic nerve, Optic tract
Ather (2019)	FA map	Optic nerve (seed/target), Chiasm (waypoint), Optic tract (seed/target)
J Puzniak (2019)	3D-MPRAGE T1w	Intersection of optic nerves (seed/target), Intersection of optic tracts (seed/target)
Takemura (2019)	3D-MPRAGE T1w	Optic chiasm (seed), LGN (target)
Lecler (2018)	NA	NA
Davies-Thompson (2013)	3D T1 TFE	Optic nerve (target), Splenium (waypoint), V1 cortex (seed)
Miller (2019)	3D T1w	Orbit (seed), Chiasm (target)
Allen (2018)	T1w	Orbit (seed), Chiasm (waypoint), LGN (target)
Altıntaş (2017)	T1w inversion recovery	Orbit (seed), Chiasm (seed), Optic tract just posterior to the chiasm (seed), LGN (seed)
Chakravarthi (2021)	NA	NA
Liang (2021)	FA map	Orbit (seed),), LGN (target)
Ho (2019)	FA map	Optic tract (5 mm behind the chiasm - seed), Chiasm (if visible - waypoint)
Jacquesson (2019)	T2w steady state	Optic chiasm (ROI), Tumor (ROE), Roof of the IV ventricle (ROE), Fibers coursing towards the cerebellum (ROE)
Wu (2019)	3D-MPRAGE T1w	Optic nerve (seed), Optic tract (seed)
Lin (2018)	NA	NA
Ma (2017)	axial T1w, axial FIESTA	Orbit (seed), Optic tract (target)
Zolal (2017)	T1w, CISS	Optic nerve adjacent to the eyeball, Chiasm
Yoshino (2016)	3D-MPRAGE T1w	Orbit (seed), LGN (waypoint), V1 cortex (endpoint)
Haijabadi (2016)	NA	Chiasm (seed), Pericalcarine and precuneus cortex (seed), Deep regions between the superior and temporal gyri latera to the trigone
Ge (2015)	3D-MPRAGE T1w	Optic nerves (multiple seeds), Chiasm
Hajiabadi (2015)	3D-MPRAGE T1w	Chiasm (seed), Lateral to the trigon (waypoint), V1 cortex (target)

Table 4 (*continued*)

Article	Sequence used as reference	Anatomic regions
De Blank (2013)	B0 image	Posterior half of the optic nerve (seed), Chiasm (target), Immediately posterior to the chiasm (seed), Immediately anterior to the LGN (target)
Lober (2012)	NA	Optic nerve (seed), Chiasm (if visible - target)
Zhang (2012)	DEC map	Optic nerve (seed), Chiasm (seed), Optic tract (near the cerebral peduncles - seed)
Hodaie (2010)	T1w FSPGR	Prechiasmtic optic nerve (seed), LGN (target)
Salmela (2009)	B0 image	Optic nerve (2 ROIs 10 mm apart), Chiasm, V1 cortex
Tao (2009)	T1w FSE	Optic nerve (seed), Chiasm (seed)
Techavipoo (2009)	T2w	Orbit (seed), Chiasm (target)
Lacerda (2021)	3D FLASH T1w	Optic nerve (seed), Chiasm (seed/target), LGN (target)
Yang (2011)	not reported	Chiasm (seed), Optic nerve (multiple seeds)

Abbreviations: DEC - diffusion encoded colors; ROE - region of exclusion; V1 - primary vision; FLASH – fast low angle shot; MPRAGE – magnetization prepared rapid gradient echo; FIESTA – fast imaging employing steady-state acquisition; CISS – constructive interference in steady-state; TFE – turbo field echo; FSE – fast spin echo; MNI – Montreal Neurlogical Institute; AP – antero-posterior.

3.7. Investigation of heterogeneity among study results

Fig. 3 shows the success rate of reconstruction in the case of direct visual assessment in patients, grouped by class of disease or health condition. A similar graph for healthy subjects was deemed superfluous as only 2/22 studies (Manners et al., 2022; Tao et al., 2009) reported success rates of <100%, although confidence intervals varied based on test sample sizes.

3.8. Risk of bias assessment

Detailed results regarding the risk of bias assessment can be found in Table 7. Very briefly, ten (25.6%) studies were considered at low risk of bias; three (7.7%) studies at medium risk of bias; and the remaining 26 (66.7%) at high risk of bias.

3.9. Protocols and outcomes in studies at low risk of bias

A summary of the studies with the highest percentage of successful reconstruction (>80%) and low risk of bias is reported in Table 6.

Regarding the acquisition, all studies were conducted using 3 T MRI, with one also using a 1.5 T scanner (Chakravarthi et al., 2021).

All studies used EPI diffusion-weighted sequences. TR ranges between 3956 ms and 17000 ms and TE between 80.8 ms and 102 ms. Voxel size ranges from a minimum of $1.25\ mm^3$ to a maximum of $2\ mm^3$ and the b value from 300 to 3000 s/mm^2, with 1000 s/mm^2 the most commonly used (5/5 entries, 100%) (Chakravarthi et al., 2021; He et al., 2021; Jacquesson et al., 2019a; Ma et al., 2016; Manners et al., 2022). Two entries performed multi-shell diffusion weighted acquisitions, but only one (Manners et al., 2022) used all the shells in the tractography processing, while the other (He et al., 2021) started from the multi-shell HCP data, but analysed only the 1000 s/mm^2 shell. The number of different gradient directions used ranges from a minimum of 24 to a maximum of 270, with 32 being the most used (2/5 entries, 40%) (Jacquesson et al., 2019a; Ma et al., 2016) and two studies (40%) classifiable as HARDI (He et al., 2021; Manners et al., 2022).

On the analysis side, 2/5 studies (40%) used deterministic algorithms (Chakravarthi et al., 2021; Ma et al., 2016) and 2/5 (40%) used probabilistic tractography (Jacquesson et al., 2019a; Manners et al.,

Table 5

Results of tractography assessment, grouped by assessment method used for the validation of the anatomical fidelity. (a) simple direct visual assessment (success/failure); (b) Direct visual assessment score; (c) Percentage of crossing fibers reconstructed; (d) Surgical evaluation, i.e. di the tract follow the anatomy visualized during surgery; (e) Other assessment methods.

(a) Direct visual assessment Article	Results	Patient population
Jin (2019)	DTI OC 0/5 (0%), OT 5/5 (100%) GQI OC 5/5 (100%), OT 5/5 (100%)	
Kammen (2016)	215/215 (Human connectome project)	
Kamali (2014)	5/5. The intraorbital segment of the optic nerve was not reconstructed	
Maleki (2012)	9/9	
Hofer (2010)	3 segments (lateral/nasal ON, OT): 5/6; 2 segments: 1/6	
Staempfli (2007)	10/10	
Manners (2022)	6/8 Pts; 12/13 HC	LHON
Takemura (2019)	7/7 Pts; 20/20 HC	LHON
Lecler (2018)	Agreement with anatomy, no chiasm visible	Congenital achiasma
Davies-Thompson (2013)	9/9 HC; agreement with anatomy and no chiasm visible in the patient	
Miler (2019)	6/6 Pts; 6/6 HC	Unilateral advanced stage glaucoma
Allen (2018)	15/15 Pts; 13/13 HC	Amblyopia
Altıntaş (2017)	15/15 Pts; 10/10 HC	Amblyopia
Liang (2021)	65/65 Pts; 33/33 HC	Hypophyseal macroadenoma
Ho (2019)	ON L: 26/29; ON R: 27/29; OT L: 28/29; OT R: 28/29	OPG
Jacquesson (2019)	5/5	Skull base tumours
Wu (2019)	20/20 Pts; 25/25 HC	Orbital space occupying lesions
Ma (2017)	5/5	Meningioma
Zolal (2017)	1/2	Meningioma
Yoshino (2016)	3/3 Pts; 288/288 HC	Hypophyseal adenoma
Haijabadi (2016)	preoperative: 3/25 intraoperative: 5/25 1 week post-op: 9/25 3 week post-op: 15/25 3 months post-op 18/25	Suprasellar tumours
Ge (2015)	ON 10/11 with 2/11 interrupted; OT 7/11	OPG
Hajiabadi (2015)	Preoperative tractography ON 1/2 (50%); OC 0/2 (0%); OT 1/2 (50%) Intraoperative tractography ON 1/2 (50%); OC 1/2 (50%); OT 2/2 (100%) Postoperative tractography ON 2/2 (100%); OC 2/2 (50%); OT 2/2 (100%)	Hypophyseal macroadenoma with ophthalmological comorbidities
De Blank (2013)	45.5/50 Pts (91/100 eyes)	OPG NF1 type
Lober (2012)	R normal 5/10, fewer fibres than normal 5/10, L normal 5/10, fewer fibres than normal 4/10, no fibres 1/10	OPG
Zhang (2012)	36/36 Pts; 30/30 HC. Compression and shift due to tumour clearly visible	Orbital tumours, occipital lobe tumours
Hodaie (2010)	4/4	CNS tumours
Salmela (2009)	HC: ON 10/10, OC 10/10, OT 10/10; Pts: ON 2/2, OC 1/2, OT 0,5/2	Paediatric suprasellar tumours
Tao (2009)	ON 27/45; OC and OT 45/45. 7/30 patients clearly presented a visible change of course due to compression by the tumour	Orbital tumours Orbital chronic inflammation
Techavipoo (2009)	16/16 Pts; 7/7 HC	Multiple sclerosis
Lacerda (2021)	4/4 Pts, 20/20 HC	Epilepsy
Yang (2011)	Full reconstruction 1/6; partial reconstruction 3/6; no reconstruction 2/6	Traumatic optic neuropathy

(b) Direct visual assessment (rating score) Article	Results	Population	Harmonised results
He (2021)	SD-Stream. DVA score 3.26 (scale 4–1) iFOD1. DVA score 2.93 UKF-1T. DVA score 2.32 UKF-2T. DVA score 1.47	HC	24.7 35.7 56.0 84.3
Akazawa (2010)	b = 700: DVA score 0.72 (Scale 0–3) b = 1400: DVA score 1.01 b = 2100: DVA score 0.78 b = 2800: DVA score 1.01	HC	24.0 33.7 26.0 33.7
Hofer (2010)	Nasal optic nerve: 2/6 XX; 3/6 X, 1/6 0 Lateral optic nerve: 5/6 XX; 1/6 X; 0/6 0 Optic tract: 6/6 XX; 0/6 X; 0/6 0	HC	58.3 91.7 100
Lin (2018)	Optic nerve: 4.00 (score 0–5) Optic chiasm: 4.12	Sellar region tumors	80.0 82.0

(c) Percentage of crossing fibers reconstructed Article	Processing variant	Population	Results	Population	Results
He (2021)	Sd-Stream iFOD1 UKF-1T UKF-2T	HC	30.6 45.3 28.1 77.6		
Manners (2022)	–	HC	49.1	LHON	52.3
Ather (2019)	–	HC	29.4	albinism	42.2
J Puzniak (2019)	DT unfiltered DT LiFE DT COMMIT-SB DT COMMIT-SZB	HC	5.8 11.0 20.3 22.5	albinism	40.5 37.0 42.0 46.3

Table 5 (*continued*)

(c) Percentage of crossing fibers reconstructed Article	Processing variant	Population	Results	Population	Results
	DT SIFT2		8.9		40.2
	CSD unfiltered		19.2		41.1
	CSD LiFE		35.9		42.3
	CSD COMMIT-SB		28.6		41.3
	CSD COMMIT-SZB		30.6		44.8
	CSD SIFT2		8.9		39.1

(d) Surgical evaluation Article	Results	Population	Harmonised results
Chakravarthi (2021)	Agreement. 24/24	skull base meningiomas	100
Jacquesson (2019)	Agreement: 5/5	skull base tumors	100
Ma (2017)	Agreement: 5/5	meningioma	100
Zolal (2017)	Agreement 1/2	meningioma	50
Ge (2015)	Agreement: 8/8	OPG	100

(e) Other evaluation methods Article	Processing variant	Population	Measure	Results
He (2021)	SD-Stream	HC	NOS	0.398
	iFOD1		NOS	0.605
	UKF-1T		NOS	0.508
	UKF-2T		NOS	0.719
Manners (2022)		HC	Dice	0.658
		LHON	Dice	0.817
Puzniak (2021)	For all participants high number of fascicles (10000 or higher) with non null LiFE score	Achiasma, albinism, chiasmatic hypoplasia	RMSE	< 2 mm
Zolal (2017)	Deterministic	HC	Dice	0.44
	Probabilistic		Dice	0.55
	Deterministic		FPR	0.22
	Probabilistic		FPR	0.04

Legend. For studies that employed direct visual assessment (DVA) of the reconstructions, the number of subjects in which they were considered adequate was reported. When a score-based visual assessment method was implemented this was reported as developed by the authors. In order to facilitate comparing the results, a harmonised result was computed for the latter method converting the score on a scale from 0 to 100 where the latter value represents a perfect reconstruction. For studies that used a surgical evaluation method, the number of subjects in whom reconstructions were judged adequate was reported. As harmonised result, the percentage of subjects in whom reconstructions were judged adequate was chosen. For the studies that computed the percentage of crossing fibers in the chiasm as a quantitative computative method, it was decided to report this data directly. The value should be compared with what was reported from histological studies (56%) (Chacko, 1948; Kupfer et al., 1967). For studies that used other quantitative computative methods, their result was reported directly. For studies performed on both patients and healthy controls, it was decided, because of the lack of comparability, to report the two results separately.

Abbreviations: Pts - patients; HC - healthy controls; ON - optic nerve; OC - optic chiasm; OT - optic tract; GCA - giant cell arteritis; OPG – optic pathway glioma; NF1 – neurofibromatosis 1; CNS – central nervous system; LHON – Leber's hereditary optic neuropathy; NOS - normalized overlap score; FPR – false positive rate; RMSE – Root mean square error; UKF - unscented Kalman filter; DT - diffusion tensor; CSD – constrained spherical deconvolution; LiFE – linear fascicle evaluation; COMMIT - convex optimization modeling for microstructure informed tractography; SIFT - spherical-deconvolution informed filtering of tractograms; DVA – direct visual assessment; GQI – generalized q-sampling imaging.

2022), with one study (He et al., 2021) running both types of algorithms.

For deterministic tractography, the cut-off value for FA / FOD amplitude (depending on the algorithm used) ranges from 0.005 to 0.18. Curvature threshold ranges between 40° to 80°. For probabilistic tractography, the cut-off value for FA / FOD amplitude (depending on the algorithm used) ranges between 0.005 and 0.3. Curvature threshold ranged between 10° to 45°.

The anatomical fidelity of the reconstructions was assessed via surgical evaluation in three studies (Chakravarthi et al., 2021; Jacquesson et al., 2019a; Ma et al., 2016) with two (Jacquesson et al., 2019a; Ma et al., 2016) also performing direct visual assessment of the reconstructions. Quantitative methods were used in two entries (He et al., 2021; Manners et al., 2022) both of which computed the number of crossing fibers reconstructed and also performed direct visual assessment. In one case (He et al., 2021) the spatial superimposition of the reconstructions was measured using the NOS while the volumes of the anterior optic pathway calculated from the tractographic reconstructions were compared with T1w-based segmentations generated from a mask drawn over the MNI atlas using the DICE coefficient. In the other study (Manners et al., 2022), the DICE coefficient was used to measure the superimposition of crossing and non-crossing fibers reconstructed in different steps in the processing workflow and merged together to create the final image.

4. Discussion

We performed a systematic review of the literature finding the combination of acquisition protocols, with TE/TR (60–157 ms / 3956–17000 ms), with diffusion-weighting schedules including 24–270 gradient directions between b = 500–3000 s/mm^2 that were equally able to successfully reconstruct the AOP with a high reported rate of success when combined with probabilistic tractography (FA/FOD threshold 0.005–0.3, angular threshold 10°- 45°) in the literature.

4.1. AOP diffusion-weighted acquisition protocol

Regarding the acquisition protocol, the majority of studies achieving 80% successful reconstructions used a high number of directions (up to 270), in agreement with current evidence suggesting that achieving a high angular resolution in the diffusion weighted image is needed in order to better track the complex architecture of white matter fibers in tractography (Roundy et al., 2012; Zolal et al., 2017). Moreover b-value of 1000 s/mm^2 was the most commonly used, as it is the most typical in clinical use. Among studies that performed a single-shell low b value (i. e., b < 1000 s/mm^2) acquisition, good results were achieved in two (Davies-Thompson et al., 2013; Kamali et al., 2014) out of three. However these studies have strong limitations regarding the assessment of outcomes: they performed only a direct visual assessment of the

Table 6
Summary data of studies at low risk of bias and achieving the highest anatomical fidelity accuracy of tractographic reconstructions.

Article	Scanner	TR/TE (ms)	voxel size (mm³)	b values (s/mm2)	Ngradient directions	Deterministictractography	Probabilistictractography	FA threshold	Curvature	Quality measurement methods	Anatomical fidelity results	Risk of bias
He (2021)	3 T	5520/89.5	1.25x1.25x1.25	1000*-2000–3000	270	SD-Stream		seed = 0.006; stop = 0.005	80°	Direct visual assessmentPercentage of crossing fibers reconstructed; Comparison of mutual spatial overlap between reconstructions by NOS method.	DVA*: 3.26Percentage of crossing fibers†: 30.6NOS‡: 0.398	low
							iFOD1	seed = 0.006; stop = 0.005	10°		DVA*: 2.93Percentage of crossing fibers†: 45.3NOS‡: 0.605	
							UKF-1 T	seed = 0.02; stop = 0.01			DVA*: 2.32Percentage of crossing fibers†: 28.1NOS‡: 0.508	
							UKF-2 T	seed = 0.02; stop = 0.01			DVA*: 1.47Percentage of crossing fibers†: 77.6NOS‡: 0.719	
Manners (2022)	3 T	4300/98	2x2x2	300–1000-2000	113	no	iFOD1	seed = 0.006; stop = 0.005	10°	Direct visual assessment; Percentage of crossing fibers reconstructed; Measure of the superimposition between crossing and non-crossing fibers using DICE coefficient	DVA•: 6/8 Pts; 12/13 HCPercentage of crossing fibers†: 52.3 Pts; 49.1 HCDICE‡: 0.817 Pts; 0.658 HC	low
Chakravarthi (2021)	3 T 1.5 T	17000/80.8	2x2x2.6	1000	24	BrightMatter Plan software	no	NA	NA	Surgical evaluation	•24/24 Pts	low
Jacquesson (2019)	3 T	3956/102	2x2x2	1000	32	no	Mrtrix 3 "tckgen"	0.3	45°	Direct visual assessment (comparison with CISS); Surgical evaluation	DVA•: 5/5 PtsSurgical evaluation•: 5/5 Pts	low
Ma (2017)	3 T	NA/NA	1.6x1.6x2	1000	32	3D Slicer software	no	0.18	0,7	Direct visual assessment; Surgical evaluation	DVA•: 5/5 PtsSurgical evaluation•: 5/5 Pts	low

We defined at low risk of bias studies that implemented quantitative computational methods or surgical evaluation of the anatomical accuracy of tractographic reconstructions. Only studies at low risk of bias were considered in this analysis.
* ranking score ranging from 1 (best) to 4 (worse); † the value should be compared with the one reported by histological studies (56%) (Chacko, 1948; Kupfer et al., 1967); ‡ ranging from 0 (worse) to 1 (best); • number of reconstructions judged to be anatomically adequate.
Abbreviations: DVA - direct visual assessment; HC – healthy control; Pts – patients; UKF - unscented Kalman filter; NOS – normalized overlap score; NA – not assessed.

Table 7

Tractography quality assessment methods used by each article included in the review, with consequent risk of bias assessment.

Article	Risk of bias assessment		Direct visual assessment	Direct visual assessment (ranking score)	% crossing fibers reconstructed	Surgical evaluation	Other evaluation methods	Quality measurement methods
He (2021)	Low	Multiple methods used to assess the anatomical fidelity. Both qualitative and computational quality methods used		●	●		●	Other: Comparison of mutual spatial overlap between reconstructions by NOS method.
Jin (2019)	High	Only direct visual assessment of the anatomical fidelity used. Same experimenter performed reconstructions and evaluations	●					
Kammen (2016)	High	Only direct visual assessment of the anatomical fidelity used. Same experimenter performed reconstructions and evaluations	●					
Kamali (2014)	Medium	Only direct visual assessment of the anatomical fidelity used. Different experimenters performed evaluations	●					superimposed on T1w image. Repeated by 2 experts
Maleki (2012)	High	Only direct visual assessment of the anatomical fidelity used. Same experimenter performed reconstructions and evaluations	●					
Akazawa (2010)	High	Only direct visual assessment of the anatomical fidelity used. Same experimenter performed reconstructions and evaluations		●				
Hofer (2010)	High	Only direct visual assessment of the anatomical fidelity used. Same experimenter performed reconstructions and evaluations	●	●				
Staempfli (2007)	High	Only direct visual assessment of the anatomical fidelity used. Same experimenter performed reconstructions and evaluations	●					
Manners (2022)	Low	Multiple methods used to assess the anatomical fidelity. Both qualitative and computational quality methods used	●		●		●	Other: measure of the superimposition between crossing and non-crossing fibers using DICE coeff
Puzniak (2021)	Low	Quantitative computational quality method used to assess the anatomical fidelity					●	Other: RMSE of the Connectome
Ather (2019)	Low	Quantitative computational quality method used to assess the anatomical fidelity			●			Percentage of crossing fibers reconstructed
J Puzniak (2019)	Low	Quantitative computational quality method used to assess the anatomical fidelity			●			ID - decussation index
Takemura (2019)	High	Only direct visual assessment of the anatomical fidelity used. Same experimenter performed reconstructions and evaluations	●					
Lecler (2018)	High	Only direct visual assessment of the anatomical fidelity used. Same experimenter performed reconstructions and evaluations	●					
Davies-Thompson (2013)	High	Only direct visual assessment of the anatomical fidelity used. Same experimenter performed reconstructions and evaluations	●					
Miler (2019)	High	Only direct visual assessment of the anatomical fidelity used. Same experimenter performed reconstructions and evaluations	●					superimposed to T1w image
Allen (2018)	High	Only direct visual assessment of the anatomical fidelity used. Same experimenter performed reconstructions and evaluations	●					superimposed on T1w image
Altıntaş (2017)	High	Only direct visual assessment of the anatomical fidelity used. Same experimenter performed reconstructions and evaluations	●					
Chakravarthi (2021)	Low	Direct comparison with ground truth anatomy performed.				●		surgical evaluation

Table 7 (*continued*)

Article	Risk of bias assessment		Direct visual assessment	Direct visual assessment (ranking score)	% crossing fibers reconstructed	Surgical evaluation	Other evaluation methods	Quality measurement methods
Liang (2021)	High	Only direct visual assessment of the anatomical fidelity used. Same experimenter performed reconstructions and evaluations	●					
Ho (2019)	High	Only direct visual assessment of the anatomical fidelity used. Same experimenter performed reconstructions and evaluations	●					
Jacquesson (2019)	Low	Two methods used to assess the anatomical fidelity	●			●		comparison with CISS
Wu (2019)	High	Only direct visual assessment of the anatomical fidelity used. Same experimenter performed reconstructions and evaluations	●					
Lin (2018)	Medium	Only direct visual assessment of the anatomical fidelity used. Different experimenters performed evaluations		●				using 3D models (16 experts)
Ma (2017)	Low	Two methods used to assess the anatomical fidelity	●			●		
Zolal (2017)	Low	Multiple methods used to assess the anatomical fidelity. Both qualitative and computational quality methods used	●			●	●	Other: DICE coeff between reconstruction and a T1w segmentation; false positive fibers rate
Yoshino (2016)	Medium	Only direct visual assessment of the anatomical fidelity used. Different experimenters performed evaluations	●					superimposed on T1w image. Repeated by 3 experts
Haijabadi (2016)	High	Only direct visual assessment of the anatomical fidelity used. Same experimenter performed reconstructions and evaluations	●					
Ge (2015)	Low	Two methods used to assess the anatomical fidelity	●			●		
Haijabadi (2015)	High	Only direct visual assessment of the anatomical fidelity used. Same experimenter performed reconstructions and evaluations	●					
De Blank (2013)	High	Only direct visual assessment of the anatomical fidelity used. Same experimenter performed reconstructions and evaluations	●					
Lober (2012)	High	Only direct visual assessment of the anatomical fidelity used. Same experimenter performed reconstructions and evaluations	●					
Zhang (2012)	High	Only direct visual assessment of the anatomical fidelity used. Same experimenter performed reconstructions and evaluations	●					
Hodaie (2010)	High	Only direct visual assessment of the anatomical fidelity used. Same experimenter performed reconstructions and evaluations	●					Comparison to known easily reconstructable structure (anterior commissure)
Salmela (2009)	High	Only direct visual assessment of the anatomical fidelity used. Same experimenter performed reconstructions and evaluations	●					
Tao (2009)	High	Only direct visual assessment of the anatomical fidelity used. Same experimenter performed reconstructions and evaluations	●					
Techavipoo (2009)	High	Only direct visual assessment of the anatomical fidelity used. Same experimenter performed reconstructions and evaluations	●					Superimposed on T1w image
Lacerda (2021)	High	Only direct visual assessment of the anatomical fidelity used. Same experimenter performed reconstructions and evaluations	●					
Yang (2011)	High	Only direct visual assessment of the anatomical fidelity used. Same experimenter performed reconstructions and evaluations	●					

Abbreviations: NOS - normalized overlap score; ROE - region of exclusion; RMSE - root mean square error; LiFE – linear fascicle evaluation; CISS – constructive interference in steady-state.

anatomical fidelity of the tractographies with one considered at high risk of bias (Davies-Thompson et al., 2013), and the other performed only on a small group of healthy subjects (Kamali et al., 2014). Indeed, when the evaluation was performed via a robust method (i.e., surgical evaluation) on a real-life clinical scenario (i.e., meningioma patients) only 1/2 of the reconstructions were considered successful (Zolal et al., 2017).

In the single study that compared reconstructions made with different b-values, no difference was found in anatomical fidelity (Akazawa et al., 2010). However, since it is well known that the angular resolution of the algorithm depends on the b-values themselves, this negative result may have occurred due to the subjective method of quantifying successful crossing fiber reconstruction.

Only five entries implemented a multi-shell protocol, with an average of 96.4% of successful reconstruction. Non multi-shell studies achieved on average 81.0% of successful reconstructions, suggesting that it is not the b-value itself but better modelling of the signal through a number of b-values that may help achieve good results, though this finding should be confirmed in further studies.

4.2. AOP diffusion tractography analysis protocol

The reconstruction of the anatomy of the anterior optic pathway is challenging, particularly at the level of the chiasm and especially when it is dislocated. This structure is small, and within the same voxels, crossing and kissing fibers, and partial volume with surrounding cerebrospinal fluid (CSF), can all be present.

Several more advanced diffusion tractography signal modeling techniques and tractography reconstruction algorithms have the potential to solve this issue.

Constrained Spherical Deconvolution (CSD) is a signal modelling algorithm which assumes that the diffusion signal can be represented as a combination of spherical functions representing different fiber orientations, by imposing constraints on the estimated orientations, can resolve complex fiber configurations, including regions with multiple fiber crossings, while requiring less data than unconstrained SD. In our review, we observed that the CSD method has been used in eleven studies. Two of them are among the ones at low risk of bias that achieved the best results in anterior optic pathway reconstruction: He et al. (He et al., 2021) and Manners et al. (Manners et al., 2022). Puzniak et al. (Puzniak et al., 2019) compared the number of reconstructed crossing fibers in the chiasm using DT-based deterministic and CSD-based probabilistic tractography algorithms. They found that CSD-based probabilistic algorithms produced a proportion of crossing fibers more similar to the known anatomy both in healthy controls and in patients with chiasmal decussation abnormalities (e.g., albinism). A study by Jin et al. (Jin et al., 2019) compared a DT-based and a GQI-based deterministic tractography pipeline using DSI-Studio TrackVis in several areas of fiber crossing, including the optic chiasm in the AOP. On visual inspection 100% of reconstructions in the optic chiasm were successful using GQI-based tractography, compared to none using the traditional DT-based tractography. Overall DT-based reconstructions tended to be missing, interrupted, incomplete, and rich in artifacts, while those obtained by GQI were relatively complete, accurate, and in accordance with the anatomical structure, showing less tendency to follow curved paths.

Regarding the tractography reconstruction algorithm algorithms used, a work by Zolal et al., (Zolal et al., 2017) compared deterministic (DSI-Studio) and probabilistic (FSL) algorithms for cranial nerve tractography both in healthy subjects and patients with intra-axial tumors that infiltrate, compress, or displace the optic nerve. They found that, overall, probabilistic algorithms perform better than deterministic ones in depicting the correct anatomical course of cranial nerves. He et al. (He et al., 2021) compared four different tractographic reconstruction algorithms: deterministic (SD-Stream, UKF-1 T and UKF-2 T) and probabilistic CSD-based (iFOD 1). UKF-2 T and iFOD1 obtained better performance than UKF-1 T and SD-Stream. More specifically iFOD1

yielded a fraction of crossing fibers (45.6%) closer to histologically obtained values of between 53 and 56% for a healthy population (Chacko, 1948; Kupfer et al., 1967), while UKF-2 T obtained a better volume correlation with T1w image-based segmentations, and a superior reconstruction according to the visual score (score: 1.47) and NOS values (0.719).

Considering only studies at low risk of bias (Table 6), we observed that both deterministic and probabilistic reconstruction algorithms achieved adequate anatomical fidelity results in both normal controls (He et al., 2021; Manners et al., 2022) and in patients (Chakravarthi et al., 2021; Jacquesson et al., 2019a; Ma et al., 2016).

Notably, both deterministic (Chakravarthi et al., 2021; Ma et al., 2016) and probabilistic tractography methods (Jacquesson et al., 2019a) appeared to achieve a similar reconstruction rate in patients with lesions displacing the AOP, thus suggesting that in applications where a qualitative and morphologic assessment of AOP is important, such as in presurgical planning of sellar/parasellar tumors, both deterministic or probabilistic reconstruction algorithms may be used. However, if a more precise estimation of the crossing fibers is needed, in order to qualitatively analyze the AOP (for example, in albino subjects or other decussation pathologies), probabilistic algorithms might be superior to deterministic ones. In fact, results from the work of He et al. (He et al., 2021) and Manners et al. (Manners et al., 2022) show that the percentage of correctly reconstructed crossing fibers is very close to values reported in the literature.

As discussed, we observed that several studies utilized deterministic approaches, which are typically implemented in more user-friendly software packages. However, most of them were only used in a limited number of occasions, making it impossible to compare them effectively. Indeed, SD-Stream, UKF-1 T, UKF-2 T, PRIDE, Tensorline, aFM, BrightMatter Plan, Mimics research 17.0, Neuro 3D, and InVivo Dynasuite are each referred only once (n = 1); 3D Slicer, and BrainLAB workstation two times (n = 2), dTV three times (n = 3), DSI-Studio and DTI-Studio are used five times (n = 5). Among the low risk of bias studies (Table 6), three out of five used a deterministic approach, two of them in patients with sellar-parasellar lesions, and all with good results, thus support to the use of a deterministic approach in a presurgical context, even if a specific package or algorithm cannot be recommended based on the available data.

Looking beyond the articles included in the present review, recently developed model-based diffusion analysis techniques, such as NODDI (Neurite Orientation Dispersion and Density Imaging;) (Zhang et al., 2012a) and DIAMOND (DIstribution of Anisotropic MicrOstructural eNvironments in Diffusion-compartment imaging) (Wilkins et al., 2015; Reymbaut et al., 2021) have the potential to solve the issue of complex intravoxel contributions to diffusion modeling. While the NODDI model assumes that water diffusion within a voxel occurs in three compartments - intracellular space, extracellular space, and cerebrospinal fluid – DIAMOND applies a more flexible multicompartment model, attempting to estimate the number of compartments from the data itself. In simulation experiments of brain diffusion data, both DIAMOND and NODDI consistently achieved significantly lower angular error levels than the DT model, especially for angles between fibers lower than 30° (Scherrer et al., 2016) This suggests that they may be better able to model areas of complex fiber architecture. NODDI has been applied successfully to the construction of the post-chiasmatic AOP but not yet to the whole pathway (Haykal et al., 2022). For this reason, we recommend the use of multishell acquisitions whenever possible to facilitate signal modeling using the more advanced algorithms, especially when tissue characterization rather than simple tract identification is the goal.

One useful finding of our review is that most studies used anatomical ROIs drawn in the same three regions (i.e., orbital segment of the optic nerve, optic chiasma, and LGN). This is reassuring, as the AOP is a well-defined anatomic structure, whose and fiber organization are well-known. (Stranding, 2020). Considering that a possible limitation of the ROI-based strategy in the clinical context is that defining the ROI at
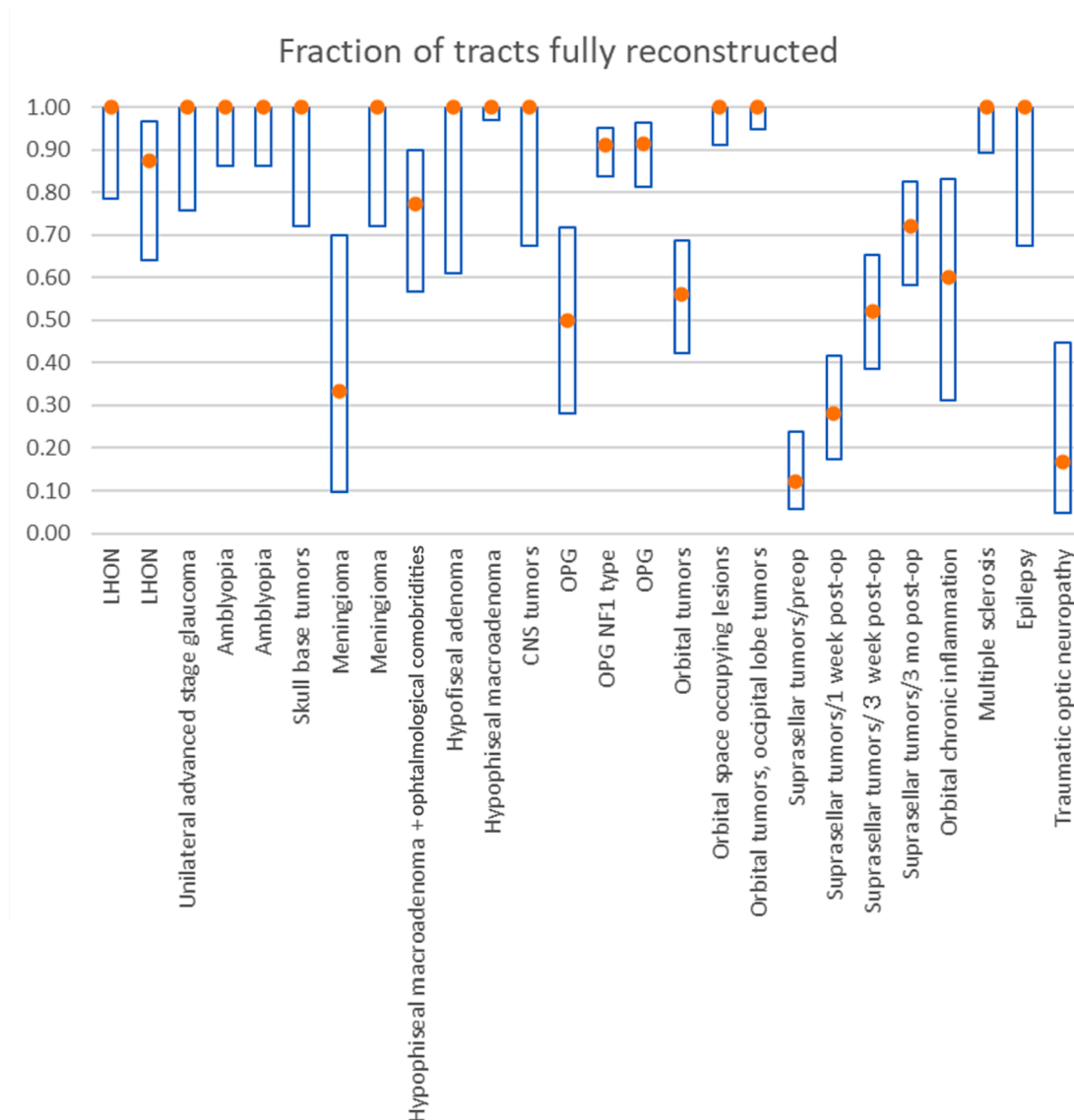
Fraction of tracts fully reconstructed

Fig. 3. Summary of the success rate of reconstruction in case of direct visual assessment of patients affected by different pathologies reported on the × axis. The central dot represents the ratio $\frac{n.reconstructed segments}{2(n.patients)}$ while the bars cover the 95% confidence interval.

the single-subject level can be very time-consuming (Jacquesson et al., 2019a) and requires a high level of experience, this standardization of ROI generation has allowed the process to be automated. In fact, several studies successfully create a standard ROI in the atlas space (Kammen et al., 2016; Maleki et al., 2012; Manners et al., 2022) or in a subsample of data (Kammen et al., 2016) and register it to the single subject space.

4.3. Study heterogeneity

Most interestingly, but unsurprisingly, our review confirmed a high level of heterogeneity in the methods used to evaluate reconstruction quality, i.e., the anatomical fidelity of the reconstructions in the absence of a commonly accepted "standard of procedure" for the objective evaluation of the tractographic reconstruction. This problem has been previously considered in depth for tracts within the brain (Maier-Hein et al., 2017; Renauld et al., 2023), but not in the case of the cranial nerves. Direct visual assessment was most commonly used. However, this approach is highly dependent on operator experience as diffusion-weighted images proximal or anterior to the chiasm suffer from both low SNR and spatial distortion. In order to properly perform visual assessment, reconstructed tracts should at least be superimposed on a

conventional MRI image, T1-weighted being the most commonly used, requiring volumetric registration (e.g., between a population T1-weighted template and individual diffusion MRI (dMRI) data) to align the two image spaces. While there are many sophisticated tools to compute these registrations such as FSL fnirt (Jenkinson et al., 2012) and ANTs (Avants et al., 2010), their performance is limited by factors such as differences in image resolution (Malinsky et al., 2013) and echo-planar imaging (EPI) distortion in dMRI data (Albi et al., 2018).

Very few studies claimed a success rate of <100% in reconstruction of the AOP of healthy subjects (Table 5). However, given the moderate number of subjects reported in many cases, it would be difficult to generalize this result. The most convincing verification was that of Kammen et al. (Kammen et al., 2016) on 215 cases. However, this was performed on subjects scanned during the Human Connectome Project, for which both scanning and quality control protocols were performed at a level above that typically found in a clinical setting. The question of what constitutes a successful tract reconstruction is important. In many cases, including the report of Kammen et al. (Kammen et al., 2016), a complete tractographic reconstruction with a plausible course was counted as a success. However, in the absence of a standard of comparison, the degree of error cannot be quantified. However, in studies

that evaluated reconstructions using a rating scale, success rates of 100% were not reported (Table 5)(b).

Tests of tractographic methods based on patient data provide more interesting, and arguably more relevant, comparative data. Fig. 3 highlights several interesting points. First of all, the overall success rate is lower than for healthy controls. A simple aggregation of the data reveals that 707 out of 896 AOPs (79%) were reconstructed. However, the aggregate result is not particularly interesting, for two reasons. First, it hides the variability related to studies examining different diseases or health conditions, and potentially different reconstruction algorithms. Secondly, in certain cases, in which vision is impaired, the reconstruction of a complete AOP would arguably not count as a successful result. In fact, in the study of Yang et al. (Yang et al., 2011), tractography was successful in only one out of six patients affected by traumatic optic neuropathy. On the other hand, the study of Haijabadi et al. (Hajiabadi et al., 2016) on parasellar tumor patients before and after surgery demonstrates that even when the AOP is intact, the proximity of other tissues with low anisotropy can create false negative findings.

So, the definition of a successful tractography depends on the use to which the results will be put. If the goal is to evaluate diffusion parameters along the tract, perhaps with the goal of deriving a biomarker to predict the response of a visual deficit to the treatment, then the definition of a complete pathway is more important than anatomical fidelity. If the goal is to determine whether the axon is intact, then a method that completes the pathway even in the absence of relevant data is not useful. If the aim is to determine the course of the tract prior to surgical removal of space-filling lesions, then a sufficient degree of anatomical accuracy is important – it should be possible to specify the position of the tract relative to the tumor or other lesion. In these cases, a reference standard is essential.

Among the studies included in this review, other than visual comparison to structural images, two main forms of standard were used (Table 7), surgical evaluation and mathematical measures of overlap between DW and high-resolution imaging. Four out of five studies using surgical evaluation reported a 100% success rate, although only the study of Chakravarthi et al. (Chakravarthi et al., 2021) reported on more than ten cases. The study of Zolal et al. (Zolal et al., 2017) reported failure in one out of two cases. The lower success rate in this study can be partially explained by the complexity of the cases: skull base meningiomas with multiple cranial nerve displacement. In particular, one of the two patients was considered by the surgeons to have the AOP severely flattened and displaced. On the other hand, this work used a single-shell b value lower than the standard clinical acquisition (i.e., b < 1000 s/mm^2) which is considered to be limited in tracking difficult fiber architecture like sharp turns or flattened and displaced nerves.

To arrive at a more objective assessment, some studies have implemented computational methods to measure the quality of the study, such as the DICE coefficient (Manners et al., 2022; Zolal et al., 2017) (He et al., 2021), NOS (He et al., 2021), LiFE score (Puzniak et al., 2019). Values were clearly influenced by the algorithm employed (He et al.,

2021), but reasonably high (over 50%), although only healthy control subjects and patients with a disease not associated with positional shift of the AOP (Manners et al., 2022) were studied. Applications in tumor cases, in which anatomical accuracy is most relevant, are missing. We believe that studies on that particular patient population are needed to allow this problem to be investigated in greater detail. It is challenging to establish a true quantitative computational method to validate the anatomical fidelity of the reconstruction. While tractography generates estimates of structural connection trajectories that are consistent with the underlying fiber orientations, it does not provide any guarantees regarding consistency between the number of such reconstructed connections with the actual number of parallel axons in a white matter region (Jones, 2010; Jones et al., 2013) Nevertheless, quantitative computational methods have the advantage of being more comparable, objective and less dependent on *a priori* knowledge of the anatomy by the operator; a possible solution would be to implement a multimodal validation strategy integrating quantitative measures with direct assessment of the ground truth anatomy, such as surgical evaluation, whenever possible (Zolal et al., 2017).

The final method of evaluation employed repeatedly in the studies reviewed uses the proportion of crossing fibers relative to uncrossed fibers in the chiasm both in healthy subjects or with decussation anomalies (Ather et al., 2019; He et al., 2021; Manners et al., 2022; Puzniak et al., 2019). It is based on the data retrieved from histological studies that demonstrated that the ratio between crossing and non-crossing fibers in the chiasm is around 56% (Chacko, 1948; Kupfer et al., 1967). He et al. (He et al., 2021) demonstrated that probabilistic algorithms achieve a result closer to that value, due to their ability to better track fiber crossings. Advanced signal modeling strategies like CSD also achieve a result closer to the ground-truth anatomy compared to the traditional DT model (Puzniak et al., 2019).

4.4. Review limitations

This study has several limitations. First of all, we have not included studies in which only a subsegment of the pathway was evaluated (i.e., only optic nerve, only optic chiasm or only optic tract) because this kind of partial reconstruction does not reflect the challenges researchers face while trying to perform the complete reconstruction of the pathway from the orbit to the geniculate ganglion. Moreover, we did not, as originally intended per the registered protocol, report microstructural data in the studies analysed because the extensive heterogeneity during acquisition did not provide comparable data for meaningful comparison.

4.5. Implications for practice and future research

Considered as a whole, the evaluation techniques employed in the studies under review are heterogeneous and vulnerable to bias. We suggest an integrated strategy to reduce the risk of bias in the future including using computational methods in the anatomical validation of

Table 8
Recommendations for measurement methods to evaluate success of tractographic reconstruction.

Purpose of tractography	Population	Method of evaluation	Result	Metric
Create ROI for evaluating diffusion parameters	HC	Compare fiber number L/R or crossing/non-crossing, per subject	Quantitative	Absolute deviation of proportion from 50%
Create ROI for evaluating diffusion parameters	HC/patients	Compare with simple atlas-based ROIs	Quantitative	*t* test of parameter; null finding indicates tract and atlas-based ROIs equivalent
Create ROI to identify AOP on EPI images	HC/patients	Voxelwise comparison with manually drawn ROIs on EPI images	Quantitative	Value of coefficient (e.g. Dice, NOS)
Create ROI to identify AOP on non-EPI images	HC/patients	Voxelwise comparison with manually drawn ROIs on non-EPI images	Quantitative	Value of coefficient (e.g. Dice, NOS)
Evaluate AOP integrity	HC/patients	Include patients with known compromised integrity in test sample	Quantitative or categorical	Normalized fiber number; success/failure of whole AOP reconstruction
Evaluate AOP displacement	Patients with space-filling lesions	Investigation during surgery	Categorical	Position of AOP relative to lesion, direction of displacement

Abbreviations: AOP - anterior optic pathway; EPI - eco planar imaging; ROI – region of interest.

reconstructions. Based on an analysis of the articles identified in this review it is possible to recommend several methods of evaluation of the anatomical fidelity of the data, differentiated based on the purpose of the tractography. These are summarized in Table 8.

It is well known that AOP tractography has the potential to assist the neurosurgical procedures of sellar and parasellar tumor removal using neuro-navigational systems (Chakravarthi et al., 2021; Jacquesson et al., 2019a; Ma et al., 2016). In fact, this technology has the potential to permit a preoperative three-dimensional visualization of the AOP and improve the presurgical planning of a patient candidate to endonasal approach (Anik et al., 2011; Hajiabadi et al., 2016; Hales et al., 2018; Liang et al., 2021; Lober et al., 2012; Yoshino et al., 2016) and his standardization could facilitate his implementation of this approach in clinical practice.

An additional benefit of a standard method of AOP tractography acquisition and processing is that this would facilitate the use of diffusion metrics that provide insights into microstructural changes within the pathway. Indeed there is evidence demonstrating their correlation with disease activity such as optic neuritis in multiple sclerosis (Dasenbrock et al., 2011; Sisto et al., 2005; Techavipoo et al., 2009), axonal degeneration in LHON (Manners et al., 2022; Takemura et al., 2019) or consequential to a primary ocular globe pathology, such as glaucoma (Miller et al., 2019). Tractography metrics are highly sensitive to the choice of the underlying acquisition parameters and fiber tracking algorithms, as well as the numbers of gradients and shells, which can further affect any quantitative metrics derived. Because of the high degree of methodological heterogeneity found in the articles under review, we decided not to extract the quantitative values of the diffusion metrics when these were reported because it would have been impossible to define normative values or infer a biological significance, limiting their value in clinical applications.

5. Conclusions

In conclusion, a satisfactory level of anterior optic tractography reconstruction has been achieved using several different combinations of acquisition parameters, with a minimum of 24 gradient directions and at least one b-value no lower than 1000 s/mm2. Both DT and CSD signal modeling methods are feasible (see Table 6 for further details). Interestingly, in patients with displacement of the AOP the quality of anatomical reconstruction reported using deterministic algorithms is not inferior to that obtained by probabilistic algorithms, so long as suitable stopping threshold and maximum curvature values are selected. Thus, deterministic algorithms may be effective for qualitative applications of AOP tractography. However, in more quantitative applications, probabilistic algorithms may be more advantageous due to their ability to represent fiber crossing areas. Advanced modeling methods may be advantageous for cases in which it is important to precisely characterize intravoxel microstructure.

To date, the anatomical fidelity of tractographic reconstruction has been evaluated mainly by direct visual assessment performed by the same operator who processed the tractographies. This method is highly subjective. We recommend that one or more objective or quantitative methods for evaluation of anatomical fidelity, depending on the purpose of the tractography and based on those already attested in the literature, should be preferred to determine the reliability of each tractographic reconstruction.

CRediT authorship contribution statement

Alessandro Carrozzi: Conceptualization, Methodology, Validation, Investigation, Writing – original draft, Data curation, Formal analysis. **Laura Ludovica Gramegna:** Conceptualization, Methodology, Validation, Investigation, Writing – original draft, Data curation, Formal analysis, Supervision, Validation. **Giovanni Sighinolfi:** Methodology, Validation, Investigation, Writing – original draft, Data curation, Formal analysis. **Matteo Zoli:** Conceptualization, Supervision, Validation. **Diego Mazzatenta:** Conceptualization, Supervision, Validation. **Claudia Testa:** Conceptualization, Supervision, Validation. **Raffaele Lodi:** Conceptualization, Supervision, Validation. **Caterina Tonon:** Conceptualization, Supervision, Validation, Supervision, Validation, Writing – review & editing. **David Neil Manners:** Data curation, Formal analysis, Validation, Writing – review & editing.

Declaration of Competing Interest

The authors declare that they have no known competing financial interests or personal relationships that could have appeared to influence the work reported in this paper.

Data availability

Data will be made available on request.

Acknowledgments

References

Agresti, A., Coull, B.A., 1998. Approximate is better than "exact" for interval estimation of binomial proportions. Amer. Statist. 52 (2), 119.

Akazawa, K., Yamada, K., Matsushima, S., Goto, M., Yuen, S., Nishimura, T., 2010. Optimum b value for resolving crossing fibers: a study with standard clinical b value using 1.5-T MR. Neuroradiology 52 (8), 723–728.

Albi, A., Meola, A., Zhang, F., Kahali, P., Rigolo, L., Tax, C.M.W., Ciris, P.A., Essayed, W. I., Unadkat, P., Norton, I., Rathi, Y., Olubiyi, O., Golby, A.J., O'Donnell, L.J., 2018. Image registration to compensate for EPI distortion in patients with brain tumors: an evaluation of tract-specific effects. J. Neuroimaging 28 (2), 173–182.

Allen, B., Schmitt, M.A., Kushner, B.J., Rokers, B., 2018. Retinothalamic white matter abnormalities in amblyopia. Investigative Ophthalmology & Visual Science 59, 921–929.

Alshowaeir, D., Yiannikas, C., Garrick, R., Parratt, J., Barnett, M.H., Graham, S.L., Klistorner, A., 2014. Latency of multifocal visual evoked potentials in nonoptic neuritis eyes of multiple sclerosis patients associated with optic radiation lesions. Investigative Ophthalmology & Visual Science 55, 3758–3764.

Altobelli, S., Toschi, N., Mancino, R., Nucci, C., Schillaci, O., Floris, R., Garaci, F., 2015. Brain imaging in glaucoma from clinical studies to clinical practice. Progress in Brain Research 221, 159–175.

Altıntaş, Ö., Gümüştaş, S., Cinik, R., Anık, Y., Özkan, B., Karabaş, L., 2017. Correlation of the measurements of optical coherence tomography and diffuse tension imaging of optic pathways in amblyopia. International Ophthalmology 37 (1), 85–93.

Anik, I., Anik, Y., Koc, K., Ceylan, S., Genc, H., Altintas, O., Ozdamar, D., Baykal Ceylan, D., 2011. Evaluation of early visual recovery in pituitary macroadenomas after endoscopic endonasal transsphenoidal surgery: Quantitative assessment with diffusion tensor imaging (DTI). Acta Neurochirurgica (Wien) 153 (4), 831–842.

Ather, S., Proudlock, F.A., Welton, T., Morgan, P.S., Sheth, V., Gottlob, I., Dineen, R.A., 2019. Aberrant visual pathway development in albinism: from retina to cortex. Human Brain Mapping 40 (3), 777–788.

Attyé, A., Jean, C., Remond, P., Peyrin, C., Lecler, A., Boudiaf, N., Aptel, F., Chiquet, C., Lamalle, L., Krainik, A., 2018. Track-weighted imaging for neuroretina: Evaluations in healthy volunteers and ischemic optic neuropathy. J. Magnetic Resonance Imaging 48 (3), 737–747.

Avants, B.B., Yushkevich, P., Pluta, J., Minkoff, D., Korczykowski, M., Detre, J., Gee, J.C., 2010. The optimal template effect in hippocampus studies of diseased populations. NeuroImage 49 (3), 2457–2466.

Backner, Y., Kuchling, J., Massarwa, S., Oberwahrenbrock, T., Finke, C., Bellmann-Strobl, J., Ruprecht, K., Brandt, A.U., Zimmermann, H., Raz, N., Paul, F., Levin, N., 2018. Anatomical wiring and functional networking changes in the visual system following optic neuritis. JAMA Neurology 75, 287–295.

Burton, C.R., Schaeffer, D.J., Bobilev, A.M., Pierce, J.E., Rodrigue, A.L., Krafft, C.E., Clementz, B.A., Lauderdale, J.D., McDowell, J.E., 2018. Microstructural differences in visual white matter tracts in people with aniridia. Neuroreport 29, 1473–1478.

Cauley, K.A., Filippi, C.G., 2013. Diffusion-tensor imaging of small nerve bundles: cranial nerves, peripheral nerves, distal spinal cord, and lumbar nerve roots–clinical applications. AJR Am. J. Roentgenol. 201 (2), W326–W335.

Cauquil, C., Souillard-Scemama, R., Labetoulle, M., Adams, D., Ducreux, D., Denier, C., 2012. Diffusion MRI and tensor tractography in ischemic optic neuropathy. Acta Neurologica Belgica 112 (2), 209–211.

Chacko, L.W., 1948. The laminar pattern of the lateral geniculate body in the primates. J. Neurol., Neurosurgery, Psychiatry 11 (3), 211–224.

Chakravarthi, S.S., Fukui, M.B., Monroy-Sosa, A., Gonen, L., Epping, A., Jennings, J.E., Mena, L.P.d.S.R., Khalili, S., Singh, M., Celix, J.M., Kura, B., Kojis, N., Rovin, R.A.,

Kassam, A.B., 2021. The role of 3D tractography in skull base surgery: technological advances, feasibility, and early clinical assessment with anterior skull base meningiomas. J. Neurol. Surg. B Skull Base 82 (05), 576–592.

Chen, D.Q., Zhong, J., Hayes, D.J., Behan, B., Walker, M., Hung, P.S., Hodaie, M., 2016. Merged group tractography evaluation with selective automated group integrated tractography. Front. Neuroanatomy 10, 96.

Dasenbrock, H.H., Smith, S.A., Ozturk, A., Farrell, S.K., Calabresi, P.A., Reich, D.S., 2011. Diffusion tensor imaging of the optic tracts in multiple sclerosis: association with retinal thinning and visual disability. J. Neuroimaging 21, e41–e49.

Davies-Thompson, J., Scheel, M., Lanyon, L.J., Barton, J.J.S., 2013. Functional organisation of visual pathways in a patient with no optic chiasm. Neuropsychologia 51 (7), 1260–1272.

de Blank, P.M.K., Berman, J.I., Liu, G.T., Roberts, T.P.L., Fisher, M.J., 2013. Fractional anisotropy of the optic radiations is associated with visual acuity loss in optic pathway gliomas of neurofibromatosis type 1. Neuro-Oncology 15 (8), 1088–1095.

Dice, L.R., 1945. Measures of the amount of ecologic association between species. Ecology 26 (3), 297–302.

Frezzotti, P., Giorgio, A., Toto, F., De Leucio, A., De Stefano, N., 2016. Early changes of brain connectivity in primary open angle glaucoma. Human Brain Mapping 37 (12), 4581–4596.

Garaci, F.G., Cozzolino, V., Nucci, C., Gaudiello, F., Ludovici, A., Lupattelli, T., Floris, R., Simonetti, G., 2008. Advances in neuroimaging of the visual pathways and their use in glaucoma. Progress in Brain Research 173, 165–177.

Garaci, F.G., Bolacchi, F., Cerulli, A., Melis, M., Spanò, A., Cedrone, C., Floris, R., Simonetti, G., Nucci, C., 2009. Optic nerve and optic radiation neurodegeneration in patients with glaucoma: in vivo analysis with 3-T diffusion-tensor MR imaging. Radiology 252 (2), 496–501.

Ge, M., Li, S., Wang, L., Li, C., Zhang, J., 2015. The role of diffusion tensor tractography in the surgical treatment of pediatric optic chiasmatic gliomas. J. Neuro-Oncology 122 (2), 357–366.

Glick-Shames, H., Backner, Y., Bick, A., Raz, N., Levin, N., 2019. The impact of localized grey matter damage on neighboring connectivity: posterior cortical atrophy and the visual network. Brain Imaging and Behavior 13 (5), 1292–1301.

Graham, S.L., Klistorner, A., 2017. Afferent visual pathways in multiple sclerosis: a review. Clin. Exp. Ophthalmol. 45 (1), 62–72.

Hajiabadi, M., Alimohamadi, M., Fahlbusch, R., 2015. Decision making for patients with concomitant pituitary macroadenoma and ophthalmologic comorbidity: a clinical controversy. World Neurosurgery 84 (1), 147–153.

Hajiabadi, M., Samii, M., Fahlbusch, R., 2016. A preliminary study of the clinical application of optic pathway diffusion tensor tractography in suprasellar tumor surgery: preoperative, intraoperative, and postoperative assessment. J. Neurosurgery 125 (3), 759–765.

Hales, P.W., Smith, V., Dhanoa-Hayre, D., O'Hare, P., Mankad, K., d'Arco, F., Cooper, J., Kaur, R., Phipps, K., Bowman, R., Hargrave, D., Clark, C., 2018. Delineation of the visual pathway in paediatric optic pathway glioma patients using probabilistic tractography, and correlations with visual acuity. Neuroimage Clin. 17, 541–548.

Hana, A., Husch, A., Gunness, V.R., Berthold, C., Hana, A., Dooms, G., Boecher Schwarz, H., Hertel, F., 2014. DTI of the visual pathway - white matter tracts and cerebral lesions. J. Visualized Experiments.

Haykal, S., Curcic-Blake, B., Jansonius, N.M., Cornelissen, F.W., 2019. Fixel-based analysis of visual pathway white matter in primary open-angle glaucoma. Investigative Ophthalmology & Visual Science 60, 3803–3812.

Haykal, S., Jansonius, N.M., Cornelissen, F.W., 2020. Investigating changes in axonal density and morphology of glaucomatous optic nerves using fixel-based analysis. Euro. J. Radiol. 133, 109356.

Haykal, S., Invernizzi, A., Carvalho, J., Jansonius, N.M., Cornelissen, F.W., 2022. Microstructural visual pathway white matter alterations in primary open-angle glaucoma: a neurite orientation dispersion and density imaging study. AJNR. Am. J. Neuroradiol. 43, 756–763.

He, J., Zhang, F., Xie, G., Yao, S., Feng, Y., Bastos, D.C.A., Rathi, Y., Makris, N., Kikinis, R., Golby, A.J., O'Donnell, L.J., 2021. Comparison of multiple tractography methods for reconstruction of the retinogeniculate visual pathway using diffusion MRI. Human Brain Mapping 42 (12), 3887–3904.

Higgins, J.P.T., Thomas, J., Chandler, J., Cumpston, M., Li, T., Page, M.J., Welch, V.A. (Eds.), 2019. Cochrane Handbook for Systematic Reviews of Interventions. Wiley.

Ho, C.Y., Deardorff, R., Kralik, S.F., West, J.D., Wu, Y.-C., Shih, C.-S., 2019. Comparison of multi-shot and single shot echo-planar diffusion tensor techniques for the optic pathway in patients with neurofibromatosis type 1. Neuroradiology 61 (4), 431–441.

Hodaie, M., Quan, J., Chen, D.Q., 2010. In vivo visualization of cranial nerve pathways in humans using diffusion-based tractography. Neurosurgery 66, 788-795; discussion 795-786.

Hofer, S., Karaus, A., Frahm, J., 2010. Reconstruction and dissection of the entire human visual pathway using diffusion tensor MRI. Front. Neuroanatomy 4, 15.

Hoffmann, M., Kaule, F., Levin, N., Masuda, Y., Kumar, A., Gottlob, I., Horiguchi, H., Dougherty, R., Stadler, J., Wolynski, B., Speck, O., Kanowski, M., Liao, Y., Wandell, B., Dumoulin, S., 2012. Plasticity and stability of the visual system in human achiasma. Neuron 75 (3), 393–401.

Hofstetter, S., Sabbah, N., Mohand-Said, S., Sahel, J.A., Habas, C., Safran, A.B., Amedi, A., 2019. The development of white matter structural changes during the process of deterioration of the visual field. Scientific Reports 9, 2085.

Jacquesson, T., Cotton, F., Attyé, A., Zaouche, S., Tringali, S., Bosc, J., Robinson, P., Jouanneau, E., Frindel, C., 2019a. Probabilistic tractography to predict the position of cranial nerves displaced by skull base tumors: value for surgical strategy through a case series of 62 patients. Neurosurgery 85 (1), E125–E136.

Jacquesson, T., Frindel, C., Kocevar, G., Berhouma, M., Jouanneau, E., Attyé, A., Cotton, F., 2019b. Overcoming challenges of cranial nerve tractography: a targeted review. Neurosurgery 84 (2), 313–325.

Jenkinson, M., Beckmann, C.F., Behrens, T.E.J., Woolrich, M.W., Smith, S.M., 2012. FSL. Fsl. Neuroimage 62 (2), 782–790.

Jin, Z., Bao, Y., Wang, Y., Li, Z., Zheng, X., Long, S., Wang, Y., 2019. Differences between generalized Q-sampling imaging and diffusion tensor imaging in visualization of crossing neural fibers in the brain. Surgical and Radiologic Anatomy 41 (9), 1019–1028.

Jones, D.K., Knosche, T.R., Turner, R., 2013. White matter integrity, fiber count, and other fallacies: the do's and don'ts of diffusion MRI. NeuroImage 73, 239–254.

Jones, D.K., 2010. Diffusion MRI: Theory. Oxford University Press, Methods and applications.

Kamali, A., Hasan, K.M., Adapa, P., Razmandi, A., Keser, Z., Lincoln, J., Kramer, L.A., 2014. Distinguishing and quantification of the human visual pathways using high-spatial-resolution diffusion tensor tractography. Magnetic Resonance Imaging 32 (7), 796–803.

Kammen, A., Law, M., Tjan, B.S., Toga, A.W., Shi, Y., 2016. Automated retinofugal visual pathway reconstruction with multi-shell HARDI and FOD-based analysis. NeuroImage 125, 767–779.

Klistorner, A., Sriram, P., Vootakuru, N., Wang, C., Barnett, M.H., Garrick, R., Parratt, J., Levin, N., Raz, N., Van der Walt, A., Masters, L., Graham, S.L., Yiannikas, C., 2014. Axonal loss of retinal neurons in multiple sclerosis associated with optic radiation lesions. Neurology 82 (24), 2165–2172.

Kolbe, S.C., Marriott, M., Walt, A., Fielding, J., Klistorner, A., Mitchell, P.J., Butzkueven, H., Kilpatrick, T.J., Egan, G.F., 2012. Diffusion tensor imaging correlates of visual impairment in multiple sclerosis and chronic optic neuritis. Investigative Ophthalmology & Visual Science 53, 825–832.

Koller, K., Rafal, R.D., Platt, A., Mitchell, N.D., 2019. Orienting toward threat: Contributions of a subcortical pathway transmitting retinal afferents to the amygdala via the superior colliculus and pulvinar. Neuropsychologia 128, 78–86.

Kuchling, J., Brandt, A.U., Paul, F., Scheel, M., 2017. Diffusion tensor imaging for multilevel assessment of the visual pathway: possibilities for personalized outcome prediction in autoimmune disorders of the central nervous system. The EPMA J. 8 (3), 279–294.

Kupfer, C., Chumbley, L., Downer, J.C., 1967. Quantitative histology of optic nerve, optic tract and lateral geniculate nucleus of man. J. Anatomy 101, 393–401.

Lacerda, L.M., Liasis, A., Handley, S.E., Tisdall, M., Cross, J.H., Vargha-Khadem, F., Clark, C.A., 2021. Mapping degeneration of the visual system in long-term follow-up after childhood hemispherectomy - a series of four cases. Epilepsy Research 178, 106808.

Lecler, A., Attye, A., Edelson, C., 2018. Congenital achiasma. J. Neuro-Ophthalmology 38, 344–346.

Lestak, J., Nutterová, E., Pitrová, Š., Krejčová, H., Bartosova, L., Forgacova, V., 2011. High tension versus normal tension glaucoma. a comparison of structural and functional examinations. J. Clinical & Experimental Ophthalmol. 2012, 52–109.

Levin, N., Dumoulin, S.O., Winawer, J., Dougherty, R.F., Wandell, B.A., 2010. Cortical maps and white matter tracts following long period of visual deprivation and retinal image restoration. Neuron 65 (1), 21–31.

Liang, L., Lin, H., Lin, F., Yang, J., Zhang, H., Zeng, L., Hu, Y., Lan, W., Zhong, H., Zhang, H., Luo, S., Mo, Y., Li, W., Lei, Y.i., 2021. Quantitative visual pathway abnormalities predict visual field defects in patients with pituitary adenomas: a diffusion spectrum imaging study. European Radiology 31 (11), 8187–8196.

Lin, J., Zhou, Z., Guan, J., Zhu, Y., Liu, Y., Yang, Z., Lin, B., Jiang, Y., Quan, X., Ke, Y., Xu, T., 2018. Using three-dimensional printing to create individualized cranial nerve models for skull base tumor surgery. World Neurosurgery 120, e142–e152.

Lober, R.M., Guzman, R., Cheshier, S.H., Fredrick, D.R., Edwards, M.S.B., Yeom, K.W., 2012. Application of diffusion tensor tractography in pediatric optic pathway glioma. J. Neurosurgery. Pediatrics 10 (4), 273–280.

Ma, J., Su, S., Yue, S., Zhao, Y., Li, Y., Chen, X., Ma, H., 2016. Preoperative visualization of cranial nerves in skull base tumor surgery using diffusion tensor imaging technology. Turkish Neurosurgery 26, 805–812.

Maier-Hein, K.H., Neher, P.F., Houde, J.C., Cote, M.A., Garyfallidis, E., Zhong, J., Chamberland, M., Yeh, F.C., Lin, Y.C., Ji, Q., Reddick, W.E., Glass, J.O., Chen, D.Q., Feng, Y., Gao, C., Wu, Y., Ma, J., He, R., Li, Q., Westin, C.F., Deslauriers-Gauthier, S., Gonzalez, J.O.O., Paquette, M., St-Jean, S., Girard, G., Rheault, F., Sidhu, J., Tax, C. M.W., Guo, F., Mesri, H.Y., David, S., Froeling, M., Heemskerk, A.M., Leemans, A., Bore, A., Pinsard, B., Bedetti, C., Desrosiers, M., Brambati, S., Doyon, J., Sarica, A., Vasta, R., Cerasa, A., Quattrone, A., Yeatman, J., Khan, A.R., Hodges, W., Alexander, S., Romascano, D., Barakovic, M., Auria, A., Esteban, O., Lemkaddem, A., Thiran, J.P., Cetingul, H.E., Odry, B.L., Mailhe, B., Nadar, M.S., Pizzagalli, F., Prasad, G., Villalon-Reina, J.E., Galvis, J., Thompson, P.M., Requejo, F.S., Laguna, P. L., Lacerda, L.M., Barrett, R., Dell'Acqua, F., Catani, M., Petit, L., Caruyer, E., Daducci, A., Dyrby, T.B., Holland-Letz, T., Hilgetag, C.C., Stieltjes, B., Descoteaux, M., 2017. The challenge of mapping the human connectome based on diffusion tractography. Nature Commun. 8, 1349.

Malania, M., Konrad, J., Jagle, H., Werner, J.S., Greenlee, M.W., 2017. Compromised integrity of central visual pathways in patients with macular degeneration. Investigative Ophthalmology & Visual Science 58, 2939–2947.

Maleki, N., Becerra, L., Upadhyay, J., Burstein, R., Borsook, D., 2012. Direct optic nerve pulvinar connections defined by diffusion MR tractography in humans: implications for photophobia. Human Brain Mapping 33 (1), 75–88.

Malinsky, M., Peter, R., Hodneland, E., Lundervold, A.J., Lundervold, A., Jan, J., 2013. Registration of FA and T1-weighted MRI data of healthy human brain based on template matching and normalized cross-correlation. J. Digital Imaging 26 (4), 774–785.

Manners, D.N., Gramegna, L.L., La Morgia, C., Sighinolfi, G., Fiscone, C., Carbonelli, M., Romagnoli, M., Carelli, V., Tonon, C., Lodi, R., 2022. Multishell diffusion MR tractography yields morphological and microstructural information of the anterior optic pathway: a proof-of-concept study in patients with leber's hereditary optic neuropathy. Int. J. Environ. Res. Public Health 19 (11), 6914.

Mascioli, G., Salvolini, S., Cavola, G.L., Fabri, M., Giovannini, A., Mariotti, C., Salvolini, L., Polonara, G., 2012. Functional MRI examination of visual pathways in patients with unilateral optic neuritis. Radiol. Res. Pract. 2012, 1–7.

Matsuo, S., Baydin, S., Gungor, A., Middlebrooks, E.H., Komune, N., Iihara, K., Rhoton, A.L., 2018. Prevention of postoperative visual field defect after the occipital transtentorial approach: anatomical study. J. Neurosurgery 129, 188–197.

Miller, N., Liu, Y., Krivochenitser, R., Rokers, B., Bhattacharya, S., 2019. Linking neural and clinical measures of glaucoma with diffusion magnetic resonance imaging (dMRI). PLoS One1 14 (5), e0217011.

Moon, Y., Yang, J.J., Lee, W.J., Lee, J.Y., Kim, Y.J., Lim, H.W., Alzheimer's Disease Neuroimaging, I., 2021. In vivo Analysis of Normal Optic Nerve in an Elderly Population Using Diffusion Magnetic Resonance Imaging Tractography. Front Neurol 12, 680488.

Naismith, R.T., Xu, J., Tutlam, N.T., Lancia, S., Trinkaus, K., Song, S.K., Cross, A.H., 2012. Diffusion tensor imaging in acute optic neuropathies: predictor of clinical outcomes. Archives of Neurology 69, 65–71.

Nucci, C., Mancino, R., Martucci, A., Bolacchi, F., Manenti, G., Cedrone, C., Culasso, F., Floris, R., Cerulli, L., Garaci, F.G., 2012. 3-T Diffusion tensor imaging of the optic nerve in subjects with glaucoma: correlation with GDx-VCC, HRT-III and Stratus optical coherence tomography findings. The British J. Ophthalmol. 96 (7), 976–980.

Ogawa, S., Takemura, H., Horiguchi, H., Terao, M., Haji, T., Pestilli, F., Yeatman, J.D., Tsuneoka, H., Wandell, B.A., Masuda, Y., 2014. White matter consequences of retinal receptor and ganglion cell damage. Investigative Ophthalmol. Visual Science 55 (10), 6976–6986.

Paul, D.A., Gaffin-Cahn, E., Hintz, E.B., Adeclat, G.J., Zhu, T., Williams, Z.R., Vates, G.E., Mahon, B.Z., 2014. White matter changes linked to visual recovery after nerve decompression. Science Translational Medicine 6, 266ra173.

Pestilli, F., Yeatman, J.D., Rokem, A., Kay, K.N., Wandell, B.A., 2014. Evaluation and statistical inference for human connectomes. Nature Methods 11 (10), 1058–1063.

Purohit, B.S., Vargas, M.I., Ailianou, A., Merlini, L., Poletti, P.-A., Platon, A., Delattre, B. M., Rager, O., Burkhardt, K., Becker, M., 2016. Orbital tumours and tumour-like lesions: exploring the armamentarium of multiparametric imaging. Insights Imaging 7 (1), 43–68.

Puzniak, R.J., Ahmadi, K., Kaufmann, J., Gouws, A., Morland, A.B., Pestilli, F., Hoffmann, M.B., 2019. Quantifying nerve decussation abnormalities in the optic chiasm. Neuroimage Clin. 24, 102055.

Puzniak, R.J., McPherson, B., Ahmadi, K., Herbik, A., Kaufmann, J., Liebe, T., Gouws, A., Morland, A.B., Gottlob, I., Hoffmann, M.B., Pestilli, F., 2021. CHIASM, the human brain albinism and achiasma MRI dataset. Scientific Data 8, 308.

Raz, N., Levin, N., 2014. Cortical and white matter mapping in the visual system-more than meets the eye: on the importance of functional imaging to understand visual system pathologies. Front. Integrative Neurosci. 8, 68.

Raz, N., Bick, A.S., Ben-Hur, T., Levin, N., 2015a. Focal demyelinative damage and neighboring white matter integrity: an optic neuritis study. Multiple Sclerosis 21 (5), 562–571.

Raz, N., Bick, A.S., Klistorner, A., Spektor, S., Reich, D.S., Ben-Hur, T., Levin, N., 2015b. Physiological correlates and predictors of functional recovery after chiasmal decompression. J. Neuro-Ophthalmol. 35, 348–352.

Reich, D.S., Smith, S.A., Gordon-Lipkin, E.M., Ozturk, A., Caffo, B.S., Balcer, L.J., Calabresi, P.A., 2009. Damage to the optic radiation in multiple sclerosis is associated with retinal injury and visual disability. Arch. Neurol. 66, 998–1006.

Renauld, E., Theberge, A., Petit, L., Houde, J.C., Descoteaux, M., 2023. Validate your white matter tractography algorithms with a reappraised ISMRM 2015 tractography challenge scoring system. Scientific Reports 13, 2347.

Reymbaut, A., Caron, A.V., Gilbert, G., Szczepankiewicz, F., Nilsson, M., Warfield, S.K., Descoteaux, M., Scherrer, B., 2021. Magic DIAMOND: Multi-fascicle diffusion compartment imaging with tensor distribution modeling and tensor-valued diffusion encoding. Medical Image Analysis 70, 101988.

Roebroeck, A., Galuske, R., Formisano, E., Chiry, O., Bratzke, H., Ronen, I., Kim, D.S., Goebel, R., 2008. High-resolution diffusion tensor imaging and tractography of the human optic chiasm at 9.4 T. NeuroImage 39, 157–168.

Romero, R.S., Gutierrez, I., Wang, E., Reder, A.T., Bhatti, M.T., Bernard, J.T., Javed, A., 2012. Homonymous hemimacular thinning: a unique presentation of optic tract injury in neuromyelitis optica. J. Neuro-Ophthalmol. 32, 150–153.

Roundy, N., Delashaw, J.B., Cetas, J.S., 2012. Preoperative identification of the facial nerve in patients with large cerebellopontine angle tumors using high-density diffusion tensor imaging. J. Neurosurg. 116 (4), 697–702.

Rutland, J.W., Padormo, F., Yim, C.K., Yao, A., Arrighi-Allisan, A., Huang, K.H., Lin, H. M., Chelnis, J., Delman, B.N., Shrivastava, R.K., Balchandani, P., 2019. Quantitative assessment of secondary white matter injury in the visual pathway by pituitary adenomas: a multimodal study at 7-Tesla MRI. J. Neurosurg. 132, 333–342.

Salmela, M.B., Cauley, K.A., Andrews, T., Gonyea, J.V., Tarasiewicz, I., Filippi, C.G., 2009. Magnetic resonance diffusion tensor imaging of the optic nerves to guide treatment of pediatric suprasellar tumors. Pediatric Neurosurg. 45, 467–471.

Scherrer, B., Schwartzman, A., Taquet, M., Sahin, M., Prabhu, S.P., Warfield, S.K., 2016. Characterizing brain tissue by assessment of the distribution of anisotropic microstructural environments in diffusion-compartment imaging (DIAMOND). Magnetic Resonance in Medicine 76 (3), 963–977.

Schmidt, M.A., Knott, M., Heidemann, R., Michelson, G., Kober, T., Dörfler, A., Engelhorn, T., Bhattacharya, S., 2018. Investigation of lateral geniculate nucleus volume and diffusion tensor imaging in patients with normal tension glaucoma using 7 tesla magnetic resonance imaging. PLoS One1 13 (6), e0198830.

Sims, J.R., Chen, A.M., Sun, Z., Deng, W., Colwell, N.A., Colbert, M.K., Zhu, J., Sainulabdeen, A., Faiq, M.A., Bang, J.W., Chan, K.C., 2021. Role of structural, metabolic, and functional MRI in monitoring visual system impairment and recovery. J. Magnetic Resonance Imaging 54, 1706–1729.

Sisto, D., Trojano, M., Vetrugno, M., Trabucco, T., Iliceto, G., Sborgia, C., 2005. Subclinical visual involvement in multiple sclerosis: a study by MRI, VEPs, frequency-doubling perimetry, standard perimetry, and contrast sensitivity. Investigative Ophthalmology & Visual Science 46, 1264–1268.

Staempfli, P., Rienmueller, A., Reischauer, C., Valavanis, A., Boesiger, P., Kollias, S., 2007. Reconstruction of the human visual system based on DTI fiber tracking. J. Magnetic Resonance Imaging 26 (4), 886–893.

Stieglitz, L.H., Ludemann, W.O., Giordano, M., Raabe, A., Fahlbusch, R., Samii, M., 2011. Optic radiation fiber tracking using anteriorly angulated diffusion tensor imaging: a tested algorithm for quick application. Neurosurgery 68, 1239–1251.

Stranding, S., 2020. Gray's Anatomy. The anatomical basis of clinical practice, 42nd ed. Elsevier.

Takemura, M.Y., Hori, M., Yokoyama, K., Hamasaki, N., Suzuki, M., Kamagata, K., Kamiya, K., Suzuki, Y., Kyogoku, S., Masutani, Y., Hattori, N., Aoki, S., 2017. Alterations of the optic pathway between unilateral and bilateral optic nerve damage in multiple sclerosis as revealed by the combined use of advanced diffusion kurtosis imaging and visual evoked potentials. Magnetic Resonance Imaging 39, 24–30.

Takemura, H., Ogawa, S., Mezer, A.A., Horiguchi, H., Miyazaki, A., Matsumoto, K., Shikishima, K., Nakano, T., Masuda, Y., 2019. Diffusivity and quantitative T1 profile of human visual white matter tracts after retinal ganglion cell damage. Neuroimage Clin 23, 101826.

Tao, X.F., Wang, Z.Q., Gong, W.Q., Jiang, Q.J., Shi, Z.R., 2009. A new study on diffusion tensor imaging of the whole visual pathway fiber bundle and clinical application. Chinese Med. J. 122, 178–182.

Techavipoo, U., Okai, A.F., Lackey, J., Shi, J., Dresner, M.A., Leist, T.P., Lai, S., 2009. Toward a practical protocol for human optic nerve DTI with EPI geometric distortion correction. J. Magnetic Resonance Imaging 30 (4), 699–707.

Touska, P., Connor, S.E.J., 2019. Recent advances in MRI of the head and neck, skull base and cranial nerves: new and evolving sequences, analyses and clinical applications. The British J. Radiol. 92 (1104), 20190513.

Wang, M.-Y., Qi, P.-H., Shi, D.-P., 2011. Diffusion tensor imaging of the optic nerve in subacute anterior ischemic optic neuropathy at 3T. AJNR Am. J. Neuroradiol. 32 (7), 1188–1194.

Wilkins, B., Lee, N., Gajawelli, N., Law, M., Lepore, N., 2015. Fiber estimation and tractography in diffusion MRI: development of simulated brain images and comparison of multi-fiber analysis methods at clinical b-values. NeuroImage 109, 341–356.

Wu, C.N., Duan, S.F., Mu, X.T., Wang, Y., Lan, P.Y., Wang, X.L., Li, K.C., 2019. Assessment of optic nerve and optic tract alterations in patients with orbital space-occupying lesions using probabilistic diffusion tractography. Int. J. Ophthalmol. 12, 1304–1310.

Yang, Q.-T., Fan, Y.-P., Zou, Y., Kang, Z., Hu, B., Liu, X., Zhang, G.-H., Li, Y., 2011. Evaluation of traumatic optic neuropathy in patients with optic canal fracture using diffusion tensor magnetic resonance imaging: a preliminary report. ORL: J. Oto-rhino-laryngol. Related Specialties 73 (6), 301–307.

Yoshino, M., Abhinav, K., Yeh, F.C., Panesar, S., Fernandes, D., Pathak, S., Gardner, P.A., Fernandez-Miranda, J.C., 2016. Visualization of cranial nerves using high-definition fiber tractography. Neurosurgery 79, 146–165.

Yu, F., Duong, T., Tantiwongkosi, B., 2015. Advanced MR imaging of the visual pathway. Neuroimaging Clinics of North America 25 (3), 383–393.

Zhang, H., Schneider, T., Wheeler-Kingshott, C.A., Alexander, D.C., 2012a. NODDI: practical in vivo neurite orientation dispersion and density imaging of the human brain. NeuroImage 61 (4), 1000–1016.

Zhang, Y., Wan, S.H., Wu, G.J., Zhang, X.L., 2012b. Magnetic resonance diffusion tensor imaging and diffusion tensor tractography of human visual pathway. Int. J. Ophthalmol. 5, 452–458.

Zolal, A., Sobottka, S.B., Podlesek, D., Linn, J., Rieger, B., Juratli, T.A., Schackert, G., Kitzler, H.H., 2017. Comparison of probabilistic and deterministic fiber tracking of cranial nerves. J. Neurosurg. 127, 613–621.

Zoli, M., Talozzi, L., Mitolo, M., Lodi, R., Mazzatenta, D., Tonon, C., 2021. Role of Diffusion MRI Tractography in Endoscopic Endonasal Skull Base Surgery. J Vis Exp.